CHALMERS
UNIVERSITY OF TECHNOLOGY

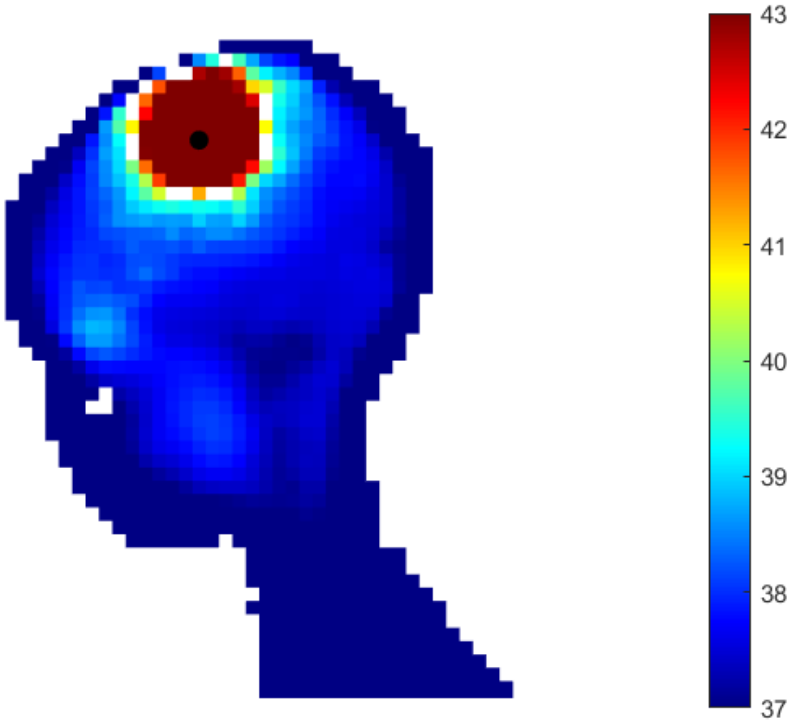

Exploring feasibility of microwave hyperthermia for pediatric brain tumors

Master's thesis in Electrical Engineering

ANNA NGUYEN
ISABELLA SYKKÖ

DEPARTMENT OF ELECTRICAL ENGINEERING
CHALMERS UNIVERSITY OF TECHNOLOGY
Gothenburg, Sweden 2024
www.chalmers.se

Master's thesis 2024

Exploring feasibility of microwave hyperthermia for pediatric brain tumors

ANNA NGUYEN
ISABELLA SYKKÖ

CHALMERS
UNIVERSITY OF TECHNOLOGY

Department of Electrical Engineering
Division of Signal Processing and Biomedical Engineering
Research group of Biomedical Electromagnetics
Chalmers University of Technology
Gothenburg, Sweden 2024

Exploring feasibility of microwave hyperthermia for pediatric brain tumors
ANNA NGUYEN
ISABELLA SYKKÖ

Supervisor: Hana Dobsicek Trefna, Department of Electrical Engineering
Examiner: Andreas Fhager, Department of Electrical Engineering

Master's Thesis 2024
Department of Electrical Engineering
Division of Signal Processing and Biomedical Engineering
Research group of Biomedical Electromagnetics
Chalmers University of Technology
SE-412 96 Gothenburg
Telephone +46 31 772 1000

Cover: Sagittal section at tumor center showing the temperature distribution in a patient model of an 11-year old with meningioma, tumor outlined in white. The black dot represents the pixel that reached the highest temperature.

Typeset in LaTeX
Printed by Chalmers Reproservice
Gothenburg, Sweden 2024

Exploring feasibility of microwave hyperthermia for pediatric brain tumors
ANNA NGUYEN
ISABELLA SYKKÖ
Department of Electrical Engineering
Chalmers University of Technology

Abstract

Brain tumors are one of the most common types of childhood cancer [1]. Microwave hyperthermia as an adjuvant treatment has the potential to improve the quality of life and survival rate of patients [2]. Hyperthermia treatment involves heating the target to $40 - 44$ °C using an antenna array. By tuning the antenna amplitude and phase, positive wave interference in the target increases tumor temperature without damaging healthy tissue. This thesis investigates the feasibility of external microwave hyperthermia for pediatric intracranial tumors. A literature review was done to investigate what tumor sizes and locations are accessible for microwave heating. Craniopharyngioma ($\approx$ 22 ml), diffuse midline glioma (H2K27M) ($\approx$ 31 ml), ependymoma ($\approx$ 49 ml), and meningioma ($\approx$ 55 ml) were identified. Simulations were performed for two study cases to investigate the final temperature distribution and the optimal operating frequency. Specific absorption rate (SAR) based treatment planning and thermal simulations were performed for frequencies between $250 - 800$ MHz with self-grounded bow-tie (SGBT) antennas. Case one investigated target size, shape, location, and tissue properties using an 11-year-old patient and a 12-channel array. The chosen tumors, a smaller ependymoma ($\approx$ 7 ml), and a skull base tumor ($\approx$ 11 ml) were tested using four different tissues: (i) healthy, (ii) average of healthy, (iii) tumor (benchmark) [3], (iv) tumor (Schooneveldt) [4]. Case two investigated the effect of different antenna arrangements within an applicator by using a 13-year-old patient with medulloblastoma (126 ml, tumor (benchmark) tissue) and both a symmetric and an optimized 10-channel array. Superficial targets, the ependymoma and meningioma, were the only ones to reach a therapeutically relevant temperature increase. Frequencies between $250 - 350$ MHz and frequency combination using $250 - 550$ MHz achieved the highest temperature exceeded by 90 % of the target volume, T_{90}, in all targets for both cases. Higher T_{90} was generally obtained for superficial tumors and for tissues with lower perfusion. A continuation of the thesis would be to investigate optimized arrays at $250 - 350$ MHz.

Keywords: microwave hyperthermia, pediatric brain tumors, hyperthermia, frequency

Acknowledgements

We would like to thank our supervisor Hana. Thank you for the opportunity to do this project, for all your ideas, and for sharing your never-ending knowledge with us. A big thanks also to Max for taking your free time to help us and explain difficult things in an easy way. Thank you Robin for always being available (and apologies for hijacking your lunch breaks). Last but not least, thank you Mattia, for being the main sponsor of our fika. It offered us a refreshing break from our thesis stress and gave us interesting conversations with all of you.

Anna Nguyen and Isabella Sykkö, Gothenburg, June 2024

List of Acronyms

List of acronyms used in this thesis listed in alphabetical order:

CBTRUS	Central Brain Tumor Registry of the United States
CNS	Central nervous system
CSF	Cerebrospinal fluid
CT	Computerized tomography
DIPG	Diffuse intrinsice pontine glioma
DMG	Diffuse midline glioma
EM	Electromagnetic
EV	Eigenvalue
GCT	Germ cell tumors
GTR	Gross total resection
HCQ	Hot-to-cold spot quotient
HGG	High-grade glioma
HR	Homologous recombination
HTV	Hyperthermia target volume
HCQ	Hot-to-cold-spot quotient
HTQ	Hot-spot to target quotient
IDH	Isocitrate dehydrogenase
IEEE	Institute of Electrical and Electronics Engineers
i-TR	Iterative time-reversal
LGG	Low-grade glioma
LR	Local refinement
MRI	Magnetic resonance imaging
MW	Microwave
PBT	Pediatric brain tumors
PEC	perfect electrical conductor
PLD	Power loss density

PML	Perfect matched layers
PS	Particle Swarm
RF	Radio-frequency
ROS	Reactive oxygen species
RS	Random search
SAR	Specific absorption rate
SEER	Surveillance, Epidemiology, and End Results
SGBT	Self-grounded bow tie
TEM	Transverse electromagnetic
TH	Thermal
UWB	Ultra-wide band
ViP	Virtual population
WHO	World Health Organisation

Nomenclature

Below is the nomenclature of constants and parameters that have been used throughout this thesis.

Constants

$h_{s,a}$	Convection coefficient between skin and air	8 $\mathrm{Wm^{-2}K^{-1}}$
$h_{s,w}$	Convection coefficient between skin and water	100 $\mathrm{Wm^{-2}K^{-1}}$
T_{air}	Air temperature	20 °C
T_{water}	Water temperature	30 °C

Parameters

c_p	Specific heat capacity
f	Frequency
Q	Perfusion rate
ε_r	Relative permittivity
κ	Thermal conductivity
λ	Wavelength
ρ	Density
σ	Electrical conductivity
x, y, z	3D cartesian coordinate system
O	origin
E	Electric field distribution
$\hat{E}$	Transformed electric field
n_p	Number of grid sampling points
η_f	Material impedance at frequency f

ω	Weight factor, used in field interpolation
$k_{i,j}$	Coupling factor between antenna i and j
U_i	Polarization axis of antenna i
T_{50}	Temperature exceeded by 50 % of the target volume
T_{90}	Temperature exceeded by 90 % of the target volume
TC_x	Iso-SAR target coverage

Contents

1 Introduction

Cancer is a common disease; around 40 % of the population will receive a cancer diagnosis in their life [1]. Over the last decades, survival rates for patients have increased [1], [5]. Yet, large variations in survival rates between cancer types remain, with brain tumors being one of the most challenging types to treat [6].

In children, brain tumors are one of the most frequent types of cancer [7]. Tumor locations vary and they can appear anywhere in the brain. A majority of malignant and low-grade benign tumors are located towards the back of the head, in the posterior fossa [8], [9]. Brain tumors are generally treated with surgery, chemotherapy, and radiation therapy [7]. The survival rate for children is generally higher than for adults, with over 75 % of all children diagnosed with cancer being cured [10]. Unfortunately, today's treatment methods cause long-term negative effects, such as cognitive impairment and growth disorders from exposing the developing brain to ionizing radiation [11].

Microwave technology has the potential to improve the quality of life and survival rate of cancer patients by enabling hyperthermia as a complementary treatment, alongside existing ones [2], [12]. Hyperthermia treatment has been found to increase both survival rate and tumor control probability for several types of cancer. In microwave hyperthermia treatment of deep-seated tumors, externally placed antennas around the body part containing the tumor send microwaves through the body. The antennas are placed in a water bolus that provides impedance matching and cools the surface of the body. Together, the antenna array and water bolus form the applicator [2]. By tuning the phase and amplitude of the waves from each antenna, the microwaves converge in the cancer tumor, with positive interference heating the target. The goal is to increase tumor temperature to 43 °C in non-invasive hyperthermia [13], [12].

In order to develop safe, reliable hyperthermia treatment, a suitable applicator is necessary. The use of ultra-wideband (UWB) systems shaped as helmets has shown a potential to improve target coverage during treatment [2]. Tumor size, alongside patient anatomy and the applicator itself, is thought to impact the optimal operating frequency of the antennas [14]. However, optimal frequencies for different brain tumors have not been exhaustively studied. Likewise, the effects of the target characteristics have not been thoroughly explored.

The thesis is structured in the following order: pediatric brain tumors are reviewed in Ch.2 with the aim of identifying suitable targets for hyperthermia. Next, the theoretical framework of hyperthermia, treatment planning, and array optimization is established in Ch.3. The methodology is outlined in Ch.4. Simulation results are introduced in Ch.5. Ch.6 discusses all results and their relation to literature before a conclusion is reached in Ch.7.

1.1 Aim and objectives

This project aims to investigate the feasibility of external microwave hyperthermia for pediatric intracranial tumors. The following questions will guide the report:

- What tumor sizes and locations are accessible for microwave heating with phased array applicators?
- How do target size, shape, location, and tissue properties affect the final temperature distribution?
- With respect to the above, and considering different antenna arrangements within the applicator, what are the optimal operating frequencies?

Expanding on the questions, first, not all targets may be equally accessible for hyperthermia treatment depending on their size and anatomical location. A small tumor requires the energy to be focused in a smaller volume compared to a larger tumor. This concentration of energy can facilitate the delivery of the necessary thermal dose, making smaller tumors more suitable for microwave heating. Superficial tumors may also be more accessible compared to deep-seated tumors as the microwaves propagate a shorter distance before reaching the target. Thus, the wave retains more energy, which allows for greater energy deposition in the tumor.

Secondly, target characteristics like size, shape, location, and tissue properties can potentially influence the temperature distribution achieved through microwave heating and the optimal operating frequency. Smaller or irregularly shaped tumors might benefit from higher frequencies because the smallest achievable focal spot of the microwaves decreases for higher frequencies, while larger tumors might require lower frequencies for adequate energy deposition. The location of a target also affects the energy deposition, with deeper seated targets possibly benefiting from lower frequencies because the penetration depth of the wave decreases for higher frequencies. Furthermore, tissue properties such as the perfusion rate and the electric conductivity could impact the heat dissipation and absorption, influencing the overall temperature distribution.

Lastly, the arrangement of antennas in the applicator may influence the optimal operating frequency. Different antenna configurations provide different heating patterns. Thus, the frequency that best achieves a uniform, high, temperature distribution in the target may vary depending on the array.

1.2 Limitations

This study is limited to brain tumors in the pediatric age group with statistics on survival rate, incidence rate, and distribution of location and histopathology from the United States. The patient model used for simulations represents the older age group in children and the literature review for finding tumor types is taking this aspect into consideration. Due to the extent of the study, it is limited to six different tumor types. Furthermore, the targets from the literature study are simplified to spherical shapes, any other model of the tumor shape is provided from the Biomedical Electromagnetics Group.

Simulations in this study take the electromagnetic and thermal aspects into account, but will not focus on fluid modeling for treatment planning. The effects of

fluid will not be considered, except for blood perfusion. Cerebrospinal fluids will be considered as a solid.

The optimal shape for the water bolus is not explored and a spherical or ellipsoidal helmet shape is used throughout the two case studies respectively. Similarly, the number of antennas in the array was predetermined to either 10 or 12 antennas based on previous research. No further analysis of the ideal number of antennas within the array is taken into account.

Single frequencies and combinations of frequencies are both considered in the study. The single frequencies are f=$[250, 275, 300, 350, 400, 450, 600, 700, 800]$ MHz. For the combination of frequencies, the range is $250 - 550$ MHz, with a step size of 100 MHz. Other frequencies and step sizes were not considered.

2

Pediatric brain tumors

This chapter provides a literature study on pediatric brain tumors (PBT). Data for pediatric tumors was mostly gathered from the Central Brain Tumor Registry (CBTRUS), an organization that gathers statistical data on primary brain and other central nervous system (CNS) tumors in the United States. This study specifically used the statistical report from CBTRUS, $2016-2020$ with survival data from the National Program of Cancer Registries (NPCR), $2001-2019$. The data was collected before the WHO classification in 2021 and will rely on the 2016 WHO Classification of Tumors of the CNS accordingly [1].

One important factor which impacts the patient survival is tumor location [15]. As such, understanding the anatomy of the brain is important. Each region of the brain has different functions and can be divided into three major regions: cerebrum, cerebellum, and brain stem. These three major regions are illustrated in figure 2.1, together with other anatomical sites. As seen in figure 2.1, the largest part of the brain is the cerebrum. The cerebrum can be divided into the right and left hemisphere and further divided into four lobes (frontal, parietal, temporal, and occipital) [16]. Following with the cerebellum, which is located in the lower back of the head and is mainly responsible for movement coordination, balance and motor learning [17]. Lastly, the brain stem is located at the back of the brain and includes the midbrain, pons, and medulla oblongata. The main functions of the brain stem are blood pressure, heart rate, breathing, and sleeping [18].

The symptoms of PBTs that arise are mostly dependent on the location of the tumor. Ataxia is common for tumors in the posterior fossa, while seizures are more commonly associated with tumors in the frontal lobe. Other symptoms such as headaches, nausea, and vision loss are usually related to intracranial pressure [19].

One important note is that PBT differs from adult tumors. Despite their resemblance in histopathology, differences in genetic and biological characteristics can arise and will affect the treatment option [21], [22]. Childhood brain tumors also tend to have a better prognosis and survival outcomes than adult tumors. Regarding tumor location, most of the PBTs occur in the brainstem and cerebellum while adult tumors occur more in the supratentorial regions [23]. The incidence of PBTs is also quite low, leading to research predominantly focusing on adult tumors and using the same treatment option for pediatric tumors [24], [22], [19].

Understanding more about the biology of PBTs has led to improved accuracy of diagnosis with progressive advancements in treatments for PBTs as well [19]. In general, the common treatment is a combination of surgery and radiation, and for many pediatric tumor types, craniospinal irradiation is more common due to its

[1] Neoplasm, unspecified, is excluded in this study as there was both little information and few population-based studies available regarding tumor size for pediatric patients.

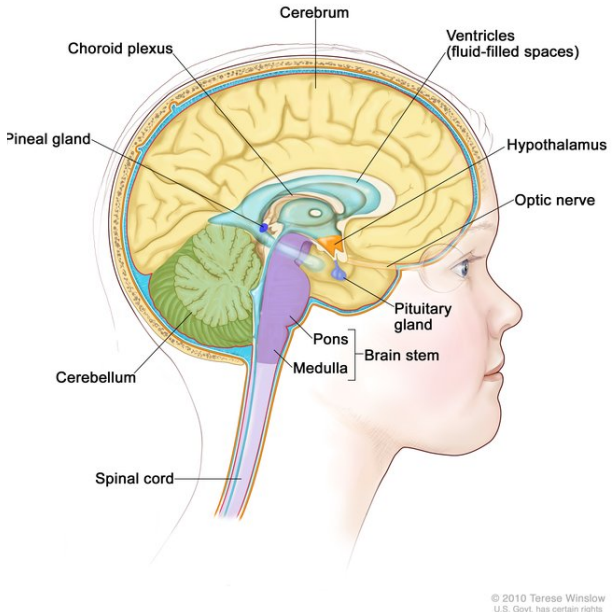

Figure 2.1: Anatomy of the brain, ©(2010) Terese Winslow LLC, U.S. Govt. has certain rights [20].

tendency to spread to nearby tissues [25]. If feasible, the initial treatment is surgery and it can either be a biopsy, subtotal resection, or gross total resection (GTR). A biopsy is a sample of tissue removed from the body and is used to determine diagnosis and treatment strategy. Secondly, subtotal resection refers to removing only a portion of the tumor to relieve pressure and is used for cases when removing the whole tumor can cause health risks for the patient. Lastly, GTR is defined as the removal of all tumor tissue detected on magnetic resonance imaging (MRI). Chemotherapy can either be an additional treatment or used for cases where you want to delay radiation therapy in younger patients [25]. The common agents include platinum agents, anti-metabolites, plant alkaloids, and alkylating agents [26].

Despite a successful treatment, it is often accompanied with long-lasting side effects [27]. There is also a wider range of side effects in children and the severity of the side effects depends largely on age and the intensity of the treatment [25].

2.1 Classification of brain tumors

The classification of brain tumors is important in order to determine prognosis and plan the initial treatment. With more progress in molecular genetics, the World Health Organization (WHO) introduced major changes in the 2021 WHO classification of tumors of the CNS [28]. These notable changes resulted in tumors being graded according to tumor types instead of across different types. Furthermore, diffuse gliomas are now categorized into adult-types and pediatric-types based on how diffuse gliomas occur primarily in each category. This means that pediatric tumors can occur in adults and vice versa, although much more rarely [29].

Even the tumor grading has changed for the 2021 WHO classification. In the past, Roman numerals have historically been used but are now replaced with Arabic numerals to minimize misreading [29], [30]. A WHO grade of $1-2$ is still considered as a low-grade tumor and a grade of $3-4$, as a high-grade tumor. More specifically, grade 1 are slow-growing, benign tumors and are often curable through surgery. Grade 2 tumors are also slow-growing but can either be benign or malignant with a risk of recurrence. Both grade 3 and grade 4 tumors are malignant and fast-growing while the latter one has an even higher chance of recurrence [31].

2.2 Distribution of histopathology and sites

The five-year total cases in the United States gathered for the distribution of pediatric brain tumors was 17136 with an annual average case of 3427. Of all reported tumors, 3.6% was the proportion for children of ages $0-14$ [32].

The figure 2.2 shows the distribution of tumor location and figure 2.3 illustrates the distribution of the different tumor types for pediatric patients between the age $0-14$. As seen in figure 2.2, the largest proportion of tumors occurred mostly in the back of the brain, with cerebellum (16.6%) and brain stem (12.6%). The rest of the tumor location is sparsely spread out in the cerebrum with the least common tumor location being meninges. From figure 2.3, the most common brain tumor in children was pilocytic astrocytoma, a low-grade glioma. In general, gliomas were the most common type of pediatric brain tumor, accounting for about 50% of all pediatric brain tumors followed by embryonal tumors at around 20% [32].

Compared with adolescents, aged $15-19$, the most frequent tumor location was in the pituitary and craniopharyngeal duct while tumors in the cerebellum and brain stem were a minority. The most common type of tumor was tumors of the pituitary, gliomas were in total around 30% while embryonal tumors were only at around 2%. See more in the appendix, figure A.3 for data regarding the distribution of tumor location for adolescents.

To summarize, there is a distinct difference between PBT and adolescent brain tumors in regard to tumor location and histology. Most of the tumors in pediatric patients occurred in the infratentorial region with a majority of tumors being gliomas. With increasing age, the majority of the tumors occur instead in the supratentorial region with tumors of the pituitary and meningioma increasing.

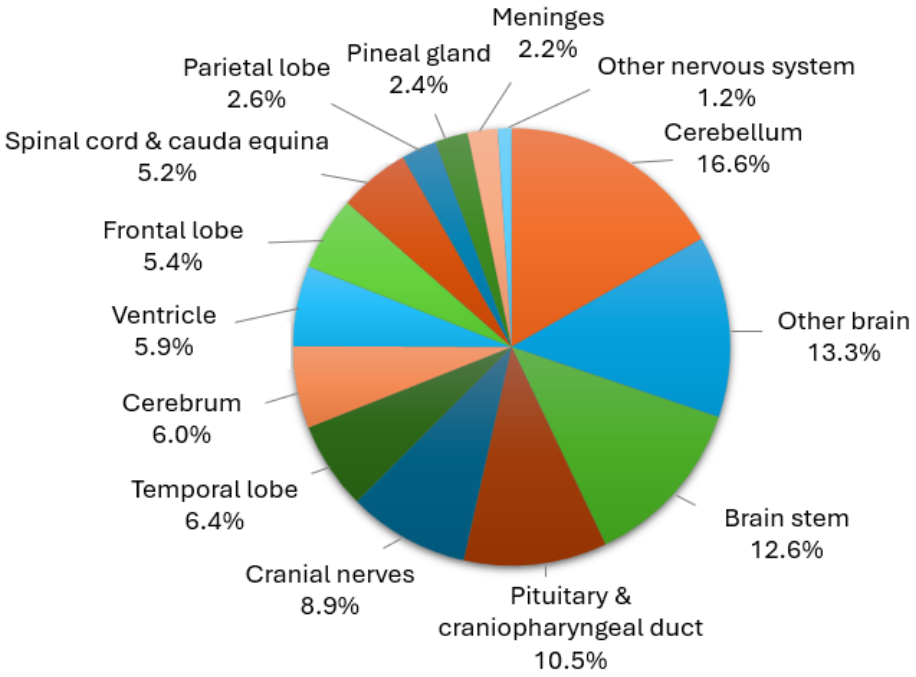

Figure 2.2: Distribution of primary brain and other CNS tumor in age group, $0-14$, by anatomical site from CBTRUS statistical report: NPCR and SEER, $2016-2020$ [32]

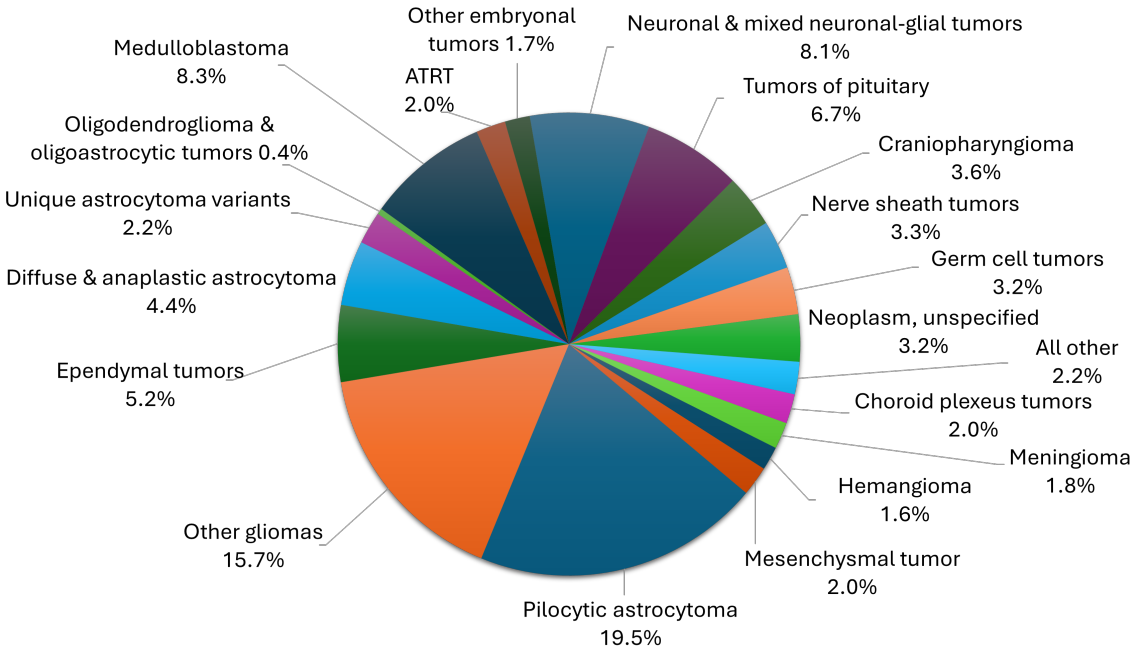

Figure 2.3: Distribution of primary brain and other CNS tumor in age group, $0-14$, based on histopathology subtypes with data from CBTRUS statistical report: NPCR and SEER, $2016-2020$ [32].

2.3 Incidence and survival rates

The incidence rates are average annual and age-adjusted per $100,000$ population of the United States. The overall incidence rate was 5.67 per $100,000$ population in the age group $0-14$, 12.00 for ages $15-39$, and 44.97 for ages 40+ years. In general, the incidence rate for brain tumors in children $0-14$ is quite low compared to adults while the relative survival rate for children had, in general, a much higher survival outcome for most of the histopathologies compared with adults[2] [32].

The figure 2.4 illustrates the incidence rate for pediatric patients in age groups $0-4$, $5-9$, and $10-14$ for different tumor types. From figure 2.4, there does not seem to be an overall pattern in regard to age and incidence rate. Some tumors seem to be more prevalent in younger children, such as ATRT and choroid plexus tumors while tumors of the pituitary while meningioma are more common in older children.

For all ages $0-14$, the highest incidence rate was a low-grade glioma, pilocytic astrocytoma. With higher grades of glioma, such as diffuse astrocytoma (grade 2), anaplastic astrocytoma (grade 3), and glioblastoma (grade 4), the incidence rate decreases. For the age group $0-4$, the lowest incidence rate was tumors of the pituitary. For the next age group $5-9$ and the oldest age group $10-14$, the lowest incidence rate was oligodendroglioma. Data regarding DMG, H3K27M (formerly DIPG), was taken from external sources where the incidence rate varied with $1-2$ per 100,000 in the United States [33] where the most common age group was $5-10$ [34].

Figure 2.5 presents the relative 1-year and 5-year survival rates for pediatric patients aged $0-14$ for respective histopathology. All of the data for survival rate is from NPCR, $2001-2019$, with the exception of DMG, H3K27M where the 1-year and 5-year survival rate was around 42% and 2% for DMG, H3K27M, respectively [35].

From figure 2.5, the survival rates are quite high for most of the tumor types. The survival and incidence rate for pilocytic astrocytoma are high and with a higher grade of glioma, both the incidence and survival rate decrease. The tumors that are desperately in need of more attention to improve outcomes are ATRT and DMG, H3K27M. Both these tumor types have a low survival rate, with DMG, H3K27M, having a major difference between the 1-year and 5-year survival rate. DMG, H3K27M, have both a low survival rate with an incidence rate varying between $1-2$ for all children, which is higher than most of the presented histopathologies.

[2]Data for DMG, H3K27M (formerly DIPG) and for the age group $0-9$ was unavailable for oligodendroglioma and meningioma from CBTRUS.

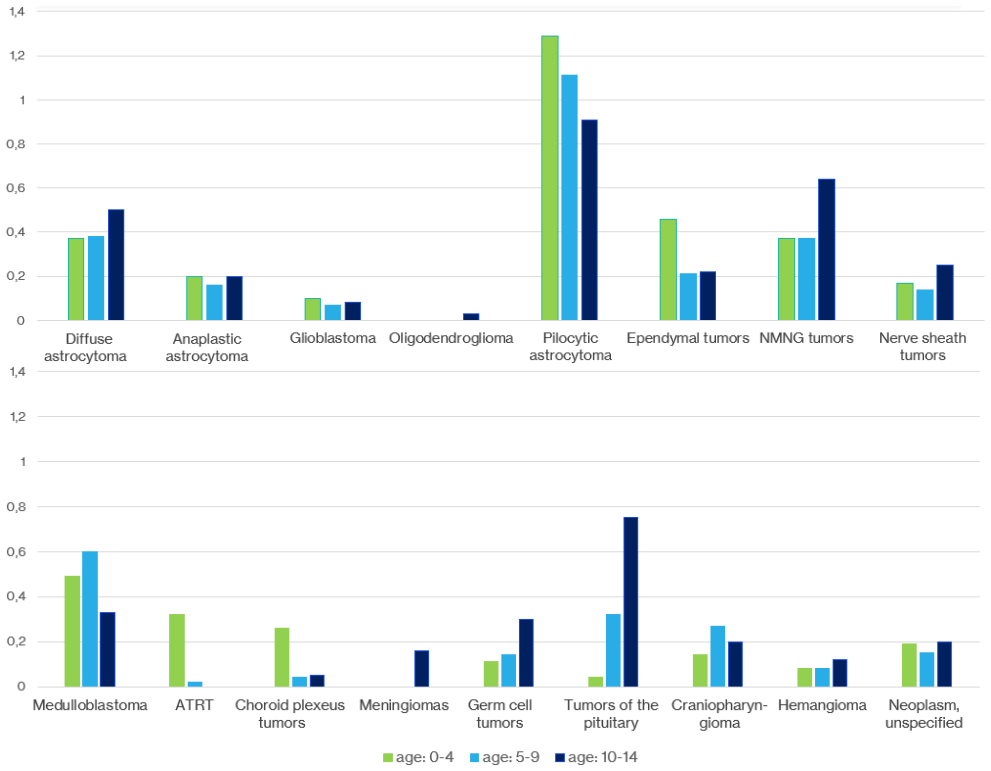

Figure 2.4: The incidence rate per $100,000$ of different tumor types in children (ages $0-14$) from CBTRUS, $2016-2020$ [32].

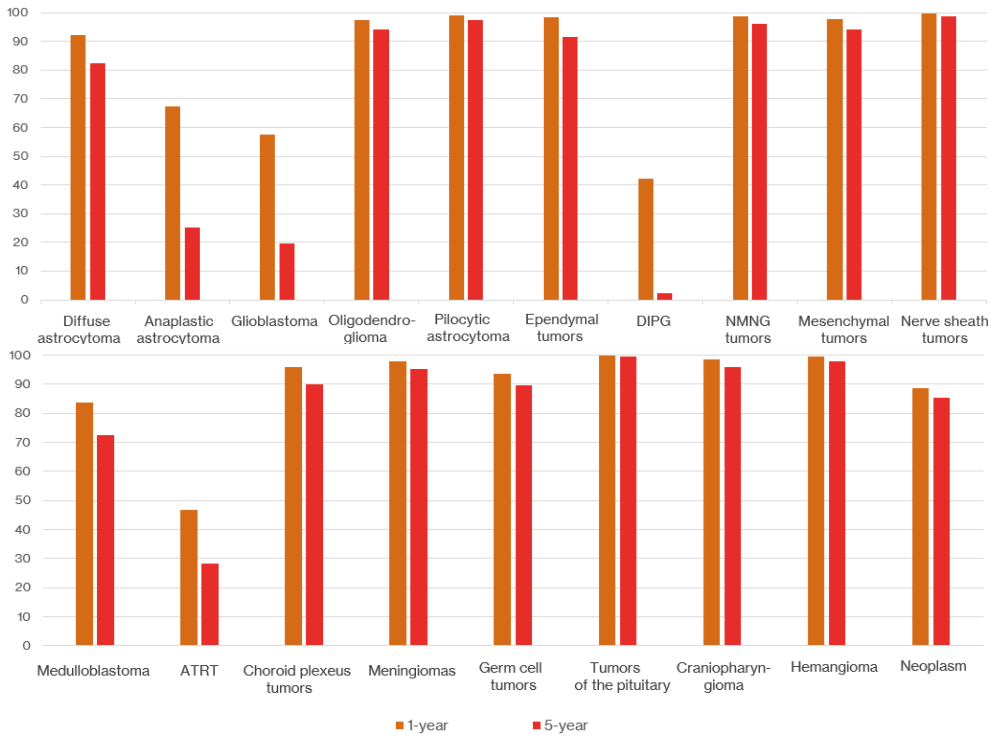

Figure 2.5: The relative survival rate of different tumor types in children (ages $0-14$) from NPCR, $2001-2019$ [32], except for DMG, H3K27M (formerly DIPG) [35].

2.4 Gliomas

Gliomas are the most common CNS tumors in children and arise from glial cells. Gliomas can be categorized into adult-type diffuse astrocytoma, pediatric-type diffuse low-grade gliomas (LGG), pediatric-type diffuse high-grade gliomas (HGG), and circumscribed astrocytic gliomas [36]. Pediatric diffuse LGG and HGG are tumors without a distinct border where HGG shows more of an aggressive behavior while circumscribed astrocytic gliomas have a clear border with a more solid growth pattern [29].

2.4.1 Astrocytoma

Astrocytoma is a type of glioma, with pilocytic astrocytoma (grade 1) and astrocytoma, IDH-mutant (grade $2-4$) as subgroups [37]. Astrocytomas develop from the star-shaped cell, called astrocytes which is a kind of glial cell [38]. Tumor location varies for astrocytomas and the grade usually increases with patient age [39].

Pilocytic astrocytoma (grade 1) is the most common low-grade glioma, categorized as circumscribed astrocytic glioma, and occurs frequently in the posterior fossa [9]. The tumor mass typically consists of an enhanced mural nodule, surrounded by a cyst. The edema around can either be mild or absent for pilocytic astrocytomas [29].

The initial treatment for low-grade astrocytomas is surgical resection and the extent of resection is one of the main prognostic factors. A greater extent of resection has been reported to improve the survival rates in patients [40], [41]. Radiation therapy is also recommended for pediatric patients when low-grade astrocytomas are progressive or if chemotherapy has failed. However, radiation therapy has been reported to correlate with long-term side effects. As such and if possible, a lower dosage and focal radiation should be used to minimize the side effects [42].

The initial treatment for high-grade astrocytomas is dependent on age. For children over three years old, the common treatment strategy is surgical resection followed by radiation therapy. The treatment strategy for children under the age of three is more challenging as radiation therapy is generally avoided and craniospinal radiation is not recommended [43]. Even chemotherapy is not an effective treatment. There have been numerous clinical trials using different chemotherapeutic agents but reported disappointing outcomes [42].

As of 2021, glioblastoma is not solely considered as an astrocytoma grade 4, and instead relies on the presence or absence of a mutation in an enzyme, isocitrate dehydrogenase (IDH). The presence and no presence of mutation in glioblastomas is called astrocytomas and IDH-wildtype glioblastoma respectively [29].

Glioblastoma in children is most commonly found in the supratentorial region and is extremely rare to occur in the cerebellum [44], [45]. The tumors are more common in adults, compared to children.

There is a difference in the molecular genetics of glioblastoma between adults and children, as well as the effectiveness of adjuvant therapies [45]. The standard treatment for pediatric patients over three years old is GTR followed by irradiation and chemotherapy using temozolomide. If GTR is not feasible, subtotal resection

is the next option. At times, subtotal resection has been reported to improve the overall survival [46].

Regarding the tumor size, a small study of 39 patients under the age of 18 years, reported a size range of $2 - 7$ cm [47]. The mean tumor size tends to increase for higher-grade astrocytoma, where Gareton, Albane et al. (2020) reported a mean tumor size of 3.6 cm for astrocytoma (grade 2) and 4.7 cm for astrocytoma (grade $3 - 4$), according to Hales, Russel K., et al. (2010). The reported mean tumor size of glioblastoma was 5.8 cm [48].

2.4.2 Diffuse midline glioma

In the past, diffuse neoplasm originating in pons was classified as diffuse intrinsic pontine glioma (DIPG) with either a H3F3A or HIST1H3B histone mutation. As of 2016, DIPG was reclassified under the category, diffuse midline glioma (DMG), with histone H3K27M mutation because it was discovered to originate from other locations as wel1 [49], [50]. The term DIPG is at times used interchangeably with DMG, H3K27M [51], [52].

DMG, H327M, is a high-grade glioma (grade 4) that develops in the pons and accounts for about 80% of all pediatric brainstem tumors [53]. The pons control vital functions such as breathing, blood pressure, and heart rate [54]. For pediatric patients, the mean tumor size using three different measurement methods was about 3.9 cm according to Hayward et al. (2008).

The origin of DMG, H3K27M is however still uncertain. One theory suggests that DMG, H3K27M, forms during the development of the cerebral tissues, as most of these tumors are more commonly found in children between the age of $5 - 10$, the age range where the cerebral tissue is actively developing [33].

DMG, H3K27M, spreads both to white and grey matter where the cells can be either small and monomorphic or large and pleomorphic [33]. Symptoms such as long tract signs and cranial palsy can quickly develop over a span of $1 - 6$ months. The pons can also expand which results in patients suffering from intracranial pressure [55].

Even with many advancements in oncology, the prognosis is still poor. Some of the challenges are the location, extensive spread of the tumor, and the intact blood-brain barrier preventing drug delivery to the target site [49]. Over the years, the patient outcome has not changed much and the survival time is less than a year [33]. As mentioned earlier, surgery is often the initial treatment for brain tumors. However, for DMG H3K27M, surgery is not always an option and no chemotherapeutic agent is currently effective [33], [56], [57]. Currently, fractionated radiation therapy is the standard treatment. There are also ongoing clinical trials of cytotoxic treatments using pre-clinical models to determine if it will improve the overall survival and quality of life [49].

2.4.3 Oligodendroglioma

Oligodendroglioma is an adult-type diffuse glioma with a WHO grade of $2 - 3$ [58]. These gliomas arise from cells called oligodendrocytes and help with produc-

ing myelin sheath covering the neurons [59]. The initial treatment is surgery, while a combination of chemotherapy and radiation is used for higher-grade or recurrent oligodendroglioma [60]. In terms of histology, pediatric and adult oligodendroglioma are quite similar [60]. As with many other pediatric brain tumors, pediatric oligodendroglioma is poorly understood regarding prognostic factors and pathology, with few studies available [58].

The unusual locations for adult oligodendrogliomas, but the common locations for pediatric oligodendrogliomas, are the brainstem, pineal region, cerebellum, and spinal cord [58]. In terms of tumor size, Lau et al. (2017) reported that the majority of oligodendrogliomas ranged from $2-4$ cm for pediatric patients, using the SEER database, $1973-2013$.

2.5 Neuronal and mixed neuronal-glial tumors

Neuronal and mixed neuronal-glial tumors (NMNG) tumors are either composed purely of neuronal or mixed neuronal and glial components. The classification of NMNG tumors has been updated since 2021 with three new tumor types added [37]. A majority of NMNG tumors are low-grade and have a small risk of showing aggressive behavior. The common symptoms are seizures, headache, nausea, and cerebellar dysfunction. Most of these tumors are located in the temporal lobe but can also occur in the infratentorial and supratentorial regions [61]. For the low-grade tumors, surgical resection is sometimes the only needed treatment, and in other cases, radiation and chemotherapy are the considered treatment [62].

The most common type of mixed neuronal-glial tumors are gangliogliomas (grade 1), which occur more frequently in children compared to adults. The physical features of these tumors are often presented as a solid-cystic mass or a solid mass with mural nodule [63]. Although these tumors may have distinct features, they are often misdiagnosed due to overlap with similar features for other tumors. The typical location is the temporal lobe but can also occur in the frontal and parietal lobes. [64]. When it comes to tumor size, it varied from $3.6-5.5$ cm for age group $1-8$ according to a small study [65].

2.6 Embryonal tumors

Embryonal tumors arise in the embryonic cells that are left from the developing stage of the fetus. These tumors are a WHO grade 4 and occur more frequently in children [30].

The most common embryonal tumor and malignant brain tumor in children is medulloblastoma [66], [67]. Medulloblastoma is categorized as an embryonal neuroepithelial tumor, an aggressive tumor that can spread throughout the CNS using the CSF pathways [68], [66]. The tumor starts growing in the fourth ventricle and can further spread to the cerebellar vermis and the brainstem. The common symptoms are increased intracranial pressure, headache, cranial nerve palsies, and ataxia [68]. Regarding tumor size, a study on 55 patients under the age of 15, reported a mean tumor size of 4.9 cm [69].

Treatment for medulloblastoma is surgical resection with a combination of chemother-

apy and radiation. As medulloblastoma has a tendency to spread to other nearby areas of the brain and along the spinal cord, craniospinal irradiation is usually the more common technique for radiation therapy. These treatments can cause long-term side effects, both neurological and cognitive dysfunction which affects up to 80% of the survivors [68].

Atypical teratoid/rhabdoid tumors (ATRT) is another type of embryonal tumor and commonly found in children below the age of 3 years old [70], [71]. The survival time is low, ranging from $6-18$ months. As with many pediatric brain tumors, ATRT is extremely rare, and not much information is available, leading to ATRT often being misdiagnosed [72]. According to a population-based study [72] with patients having a median age of one year, the most frequent location was the cerebellum, and a majority of the tumors were larger than 4 cm in diameter.

2.7 Ependymal tumors

Ependymomas are classified as WHO grade $2-3$ and arise from the ependymal cells in either the spinal cord, lining of the ventricles, or the cortical rests [28]. They are typically presented as well-demarcated, solid soft tumors. As with many other pediatric brain tumors, the primary treatment for ependymoma is GTR. Many studies also reported that the extent of resection was a great prognostic factor. With cases needing a second surgery, adjuvant radiation therapy is given [73]. For cases in which GTR is not possible, focal conformal radiotherapy is chosen for postoperative management and a study has shown great response [74].

The tumor location for ependymomas is age-dependent. For pediatric ependymomas, most of the tumors occur in the intracranial regions while adult ependymomas occur more in the spinal cord [73]. For supratentorial ependymomas, the most common signs are headache and seizures while the more common symptoms for infratentorial ependymomas are increased cerebral pressure and ataxia [75], [76]. The median tumor size is 4.45 cm, ranging from $2.2-10.0$ cm, as reported by Ruangkanchanasetr et al. (2019).

2.8 Meningioma

Meningioma has a WHO grade of $1-3$ where grade 1 is considered benign, grade 2 as atypical and grade 3 as anaplastic/malignant. Children usually have a higher grade meningioma with atypical locations, a larger tumor size, and a higher chance of recurrence [77], [78]. The symptoms vary depending on the location and size but the most common ones are headache and epilepsy [77]. Regarding location, several studies reported that meningioma occurs more in the supratentorial regions and the skull base [79], [80]. According to a population-based study, the mean tumor size for the age group $2-14$ was around 5 cm [81].

In terms of histopathology, the common ones are meningothelial and transitional meningioma [77]. The optimal treatment for meningioma is GTR to reduce the risk of recurrence but it can be challenging due to these tumors occurring close to vital structures. Meningioma also tends to grow slowly with unnoticed symptoms. This leads to a diagnosis where the tumor is already presented at a large size, adding

another level of difficulty for surgery [77].

As with many other pediatric tumors, pediatric meningioma is poorly understood regarding their clinical characteristics, radiological features, and long-term outcomes [79].

2.9 Craniopharyngioma

Craniopharyngioma is considered one of the most complex pediatric brain tumors and has a high chance of recurrence. Surgery can also be difficult due to its anatomical location [82], [83]. There are two theories regarding the origin of craniopharyngioma: the metaplastic and embryonic theory. These theories are related to the two subtypes of craniopharyngioma, papillary craniopharyngioma and adamantinomatous craniopharyngioma respectively, where the former one occurs exclusively in adults [84].

Craniopharyngioma is a benign tumor and occurs mostly in the suprasellar region. These tumors affect the visual and hypothalamic function and can cause headaches. Although the survival rates are great, the effects from treatment can lead to long-term side effects and at times, lead to premature death [85].

Currently, there is ongoing discussion regarding the optimal treatment for pediatric patients with craniopharyngioma but the main goal is to provide symptom relief and prevent tumor metastasis [22]. For most pediatric brain tumors, GTR is the standard treatment but for craniopharyngiomas, high morbidity rates have been shown to correlate with aggressive GTR. Therefore, postoperative irradiation is considered an option for treatment before surgery [86].

2.10 Choroid plexeus tumors

Choroid plexus tumors are intraventricular neoplasms and arise from the neuroepithelial lining of the ventricular choroid plexuses [87], [88].

The most notable change from WHO classification in 2021 compared with classification in 2016 is that choroid plexus tumors are considered as a separate group from the glial and glioneuronal neoplasms [89]. Choroid plexus tumors have a WHO grade of $1-3$, with papillomas (grade 1), atypical (grade 2) and carcinomas (grade 3). Choroid plexus tumors are generally quite rare and occur more in infants and younger children [90]. Former studies have shown a prevalence of choroid plexus tumors in females, with 3.5 years being the median age of diagnosis [91].

The physical appearance of choroid plexus papilloma is well-defined in a rounded shape with a cauliflower-like appearance [90]. Again, the symptoms vary depending on the tumor location but can either be focal neurological deficits or increased intracranial pressure [90] [92]. In terms of tumor size, a small population-based study reported a mean size of 4.2 cm [93].

Due to the rarity of the tumor, little information regarding treatment is available. However, GTR is reported to be favorable for papillomas but with carcinomas, only about 50% of patients have been successfully treated with GTR. Carcinomas have a tendency to reoccur and as such, adjunctive chemotherapy is given as an alternative treatment [91], [90].

2.11 Germ cell tumors

Germ cell tumors (GCT) arise from germ cells in their early developmental stages and occur mostly in the testis and ovaries but can also occur in extracranial and intracranial regions [94]. The majority of intracranial germ cell tumors occur in pediatric and adolescent patients [95].

The clinical signs can vary, from increased intracranial pressure to hypothalamic dysfunction and isolated growth hormone deficiency [96]. According to a systematic review including 218 patients between the ages $3 - 24$, the most frequent location was the pineal and the suprasellar regions [95]. For the tumor size, Greenfield et al. (2016) reported a range of $0.9 - 6.0$ cm with a mean size of 3 cm for 20 patients in the age group, $3 - 16$ years old.

GCTs can further be divided into two subcategories: germinomas and nongerminomatous germ cell tumors. Germinomas account for about $65\% - 75\%$ and the rest is nongerminomatous germ cell tumors [97]. Germimomas have both a better prognosis and a lower chance of recurrence compared to non-germinomas [98].

The treatment for pediatric GCT is chosen empirically from adult GCTs and the current treatment which are effective for germinomas is radiation therapy [96]. A combination of chemotherapy followed by craniospinal irradiation is usually the standard treatment for metastatic non-germinomas while the optimal treatment for local non-germinomas remains unclear. Using a combination of chemotherapy followed by craniospinal irradiation has been reported to improve patient outcomes compared to only using chemotherapy, which had a successful cure rate of less than 50% [98].

2.12 Mesenchymal tumor

Mesenchymal tumors are categorized into soft-tissue tumors and chondro-osseous tumors with a WHO grade $1-3$ [89]. The majority of mesenchymal tumors occurs in the supratentorial sites [99]. The only notable change in the 2021 WHO classification was the addition of three newly identified intracranial soft-tissue tumors [89].

The main treatment for mesenchymal tumors is surgical resection with an exception for rhabdomyosarcoma, where the improved survival rate is correlated with the use of radiation and chemotherapy [100]. More specifically for chondro-osseous tumors, the treatment options include different combinations of surgery, radiation therapy, and chemotherapy [101].

A study about soft-tissue tumors in children found that around 52.8% were smaller than 5 cm in size and that surgical resection was an important factor in improving overall survival [102].

2.13 Nerve sheath tumor

Nerve sheath tumors are grade 1 tumors and the most common types are schwannomas and neurofibromas. These tumors are more rare in the pediatric group, compared to adults [103]. Nerve sheath tumors occur in the tissues that protect nerve cells and can occur anywhere on the body [104].

Neurofibromas are the most common benign peripheral nerve sheath tumors and are composed of differentiated neoplastic Schwann cells and of non-neoplastic components [105]. These tumors have a very low risk of becoming malignant peripheral nerve sheath tumors [106]. The physical appearance of neurofibromas is either soft, skin-colored papules or as round, firm deep-seated lesions in the skin. As with many other brain tumors, surgery is the main treatment for nerve sheath tumors [106].

Schwannomas are composed of Schwann cells which provide support to the nervous system. Schwannomas are also benign with a low risk of turning malignant. The treatment options consist of surgery and radiation therapy where the preferable treatment depends on the location and the tumor growth rate [107].

Due to extremely few population-based studies, information regarding tumor size could not be found.

2.14 Hemangioma

Hemangioma are a group of benign tumors that can occur anywhere in the body but mostly on the surface of the skin. The physical features are various, both in shape and color. The chance of a malignant hemangioma is low and most of hemangiomas require no treatment. The cases requiring surgery are when the tumor lies deeply in the muscle or bone or on the skin and disrupts either vision, breathing, or eating. A type of hemangioma called infantile hemangioma is commonly presented within the first weeks to a few months of age, but can also be present at birth. Some cases with infantile hemangioma may regress by itself and require no treatment [108].

Population-based studies regarding brain tumor size for hemangioma in pediatric patients could unfortunately not be found.

3

Theory

This chapter overviews hyperthermia therapy, covering its rationale and applications. Then, the following chapter describes how the treatment can be planned and verified. Lastly, the final chapters cover applicator design and how an optimal antenna array can be obtained.

3.1 Hyperthermia

Hyperthermia treatment involves heating the tissue temperature to between $40-44$ °C using thermal energy [109]. This temperature range affects the cancerous cells without harming the non-cancerous cells. Multiple mechanisms are triggered in the tumor micro-environment which can improve the effectiveness of other cancer treatments, making hyperthermia useful as an adjuvant therapy [110]. An illustration of the mechanisms can be seen in figure 3.1. As seen in figure 3.1, the mechanisms include stimulation of the immune response, inhibited homologous recombination (HR) DNA repair, DNA double-strand breaks and increased reactive oxygen species (ROS) production [111], [112].

The target volume and target depth are dependent factors for heat delivery. There are three categories for target volume which are local hyperthermia, loco-regional hyperthermia and whole-body hyperthermia [113]. Regarding target depth, there are superficial heating, deep heating, interstitial heating, intracavitary heating, and perfusion-based heating. Superficial heating refers to heating a target up to a depth of 4 cm, while deep heating heats a target beyond 4 cm. Interstitial heating uses tiny applicators placed into the target volume while intracavitary heating can at

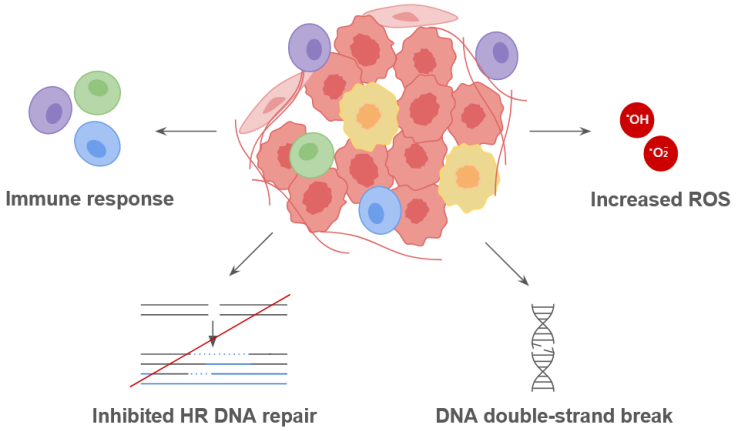

Figure 3.1: Mechanisms in the tumor micro-environment that are triggered by hyperthermia treatment.

times use applicators with a larger diameter, placed into the body's cavities. Lastly, perfusion-based heating refers to injecting a heated solution of an anticancer drug directly into the blood vessels that are either connected to the tumor or to the target region [114].

Heating can be delivered using external or internal devices with either microwave, radiofrequency (RF), ultrasound or infrared radiation [115]. Both internal and external heating uses applicators which consist of antennas. The main difference is that internal heating uses antennas placed directly into the tumor while applicators in external heating uses multi-element antenna phased arrays placed outside of the body [116]. Furthermore, a water bolus is also placed between the patient and the antennas to cool down the surface of the skin [117].

3.1.1 Deep microwave heating

Having established the general principles of hyperthermia, deep microwave heating can be explored. In deep microwave hyperthermia, external antennas generate an alternating sinusoidal electromagnetic field that delivers energy that heat a target typically located deeper from the body surface [114]. The antennas radiate through a water bolus that is placed around the target area of the patient to cool the skin and provide an impedance match between the body and the antenna [2]. Figure 3.2a show the setup from left to right. The first image is of the patient, while the second image is of the patient together with the water bolus. The third image show the addition of antennas to the bolus to form the applicator, and in the last image, the antennas radiate. To achieve deep heating, the antenna array must be a phased array system, shown in figure 3.2b. All antennas simultaneously radiate, creating a focal region due to positive interference of the electromagnetic waves. The focal spot can be steered by changing the amplitude and phase of each antenna.

Depending on which operating frequency is used, the size of the focal spot and the penetration depth varies [2]. Antennas can operate either in a single frequency or over multiple frequencies like in UWB systems. The smallest achievable focal spot scales around $\lambda/2$ to $\lambda/3$ where λ, ($\lambda = c/f$), denotes the wavelength, meaning higher frequencies f enable smaller focal spots. With higher frequencies, the penetration depth also decreases. A UWB system that combines high and low frequencies could support both focused heating and sufficient penetration depth [2].

The antenna arrangement within the applicator and the number of antennas can vary [2]. A common arrangement for applicators targeting head and neck tumors is a ring array where the antennas are equidistantly placed in one or more rings around the head. If more than one antenna is present, a mutual coupling between the antennas can occur [2]. Mutual coupling is an interaction between antennas in close proximity. As antennas are both transmitters and receivers, one antenna transmitting will affect all nearby antennas as they receive the signal.

For successful hyperthermia treatment, enough energy needs to be deposited in the target [2]. The entire target volume needs to be covered with a sufficient thermal dose, as the thermal dose is related to treatment outcome. To achieve sufficient coverage that heats the target without damaging healthy tissue, hyperthermia treatment planning is important [2].

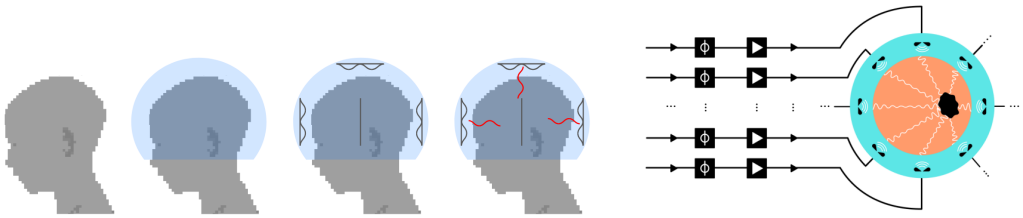

(a) Setup **(b)** Phased array

Figure 3.2: Visualization of deep microwave heating. (a) the overall setup with patient (grey), water bolus (blue) and antennas (brown) that radiate (red). (b) Top view of microwave system heating a target (black) using a phased array with black antennas in the blue bolus. Figure (b) is open access (CC BY 4.0), reprinted with permission from H. Dobsicek Trefna, available from: http://www.esho.info/.

3.2 Treatment planning

The goal of treatment planning is to achieve a high temperature in the tumor and keep the healthy tissue at physiological temperatures [2]. Constructive wave interference in the target results in the heating of the tumor. However, positive wave interference can also occur in healthy tissue surrounding the target, resulting in undesirable hot spots.

Figure 3.3 illustrates the multiple steps within the treatment planning. First, image data from a patient is segmented, yielding a patient model. Next, a treatment setup is modeled with the patient, water bolus, and antenna array. Then, the setup is used for electromagnetic (EM) simulations where the electric fields from the antennas are obtained. Field simulations are a lengthy process that can take hours to days. The fields are used in combination with algorithms to determine the optimal amplitude and phase of each antenna, called the steering parameters. Using the optimal steering parameters and the treatment setup model, thermal (TH) simulations are done to obtain a temperature distribution in the patient. Optimization is done to tune the power of the antennas.

Expanding on the last steps in treatment planning, there are many methods available to optimize the steering parameters. The two main categories of methods are based on temperature or specific absorption rate (SAR) [14]. Temperature-based methods would be ideal since temperature change is the goal, but the current lack of accurate thermal tissue properties reduces its advantages [14]. The following sections provide a deeper understanding of SAR-based treatment planning.

3.2.1 Electromagnetic simulation and optimization

Electromagnetic simulations are done to determine the SAR in a treatment setup. The SAR describes the amount of energy absorbed in terms of power loss per unit mass of tissue

$$\mathrm{SAR}_f = \frac{\sigma_f}{2\rho}|E_f|^2, \tag{3.1}$$

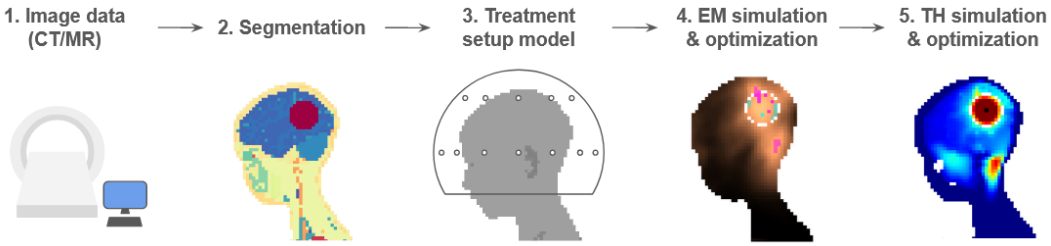

Figure 3.3: Overview of the different steps in microwave hyperthermia treatment planning. 1. A computer tomography (CT) scanner and a computer. 2. Patient model segmented into differently colored tissue groups. 3. Patient with outlined water bolus and antennas represented as white dots with grey outline. 4. SAR distribution in patient model. 5. Temperature distribution in patient model.

where σ_f is the tissue conductivity at frequency f, ρ is the density of the tissue, and E_f is the electric field at frequency f [2]. SAR-based treatment planning assumes that the SAR distribution can be used to determine the resulting temperature distribution, although the relation is non-linear [2]. The SAR-based methods do not allow for direct optimization over thermal tumor coverage.

There are many different SAR-based optimization algorithms that can be used to determine optimal steering parameters, including Eigenvalue (EV), Particle Swarm (PS), and iterative time-reversal (i-TR) [14]. EV maximizes the ratio between the average SAR in the target volume and the remaining tissue. PS minimizes the hot-spot to target quotient (HTQ). i-TR uses the SAR distribution to minimize the hot-to-cold spot quotient (HCQ) [14]. The i-TR algorithm has been tested for microwave hyperthermia and has shown to be comparable to other methods whilst being significantly faster. HTQ and HCQ are more extensively covered in section 3.2.3 as they can be both cost functions during SAR-based optimization and treatment quality indicators.

3.2.2 Thermal simulations

Having determined the optimal steering parameters, the resulting SAR distribution can be used to calculate the temperature distribution in the patient, step five in figure 3.3 [2]. Penne's bioheat equation is a common method used as a thermal model to determine the temperature in tissue that undergoes hyperthermia treatment. It is described as [118]:

$$\rho_t c_t \Delta \frac{\partial T_t}{\partial t} = k_t \Delta^2 T + \omega \rho_b c_b (T_b - T_t) + Q + \frac{\text{SAR}}{\rho}, \tag{3.2}$$

where ρ_t and ρ_b are density of the tissue and blood respectively, c_t and c_b are the specific heat capacity of the tissue and blood respectively, T_t and T_b are the temperature of the tissue and blood respectively, k is the thermal conductivity of the tissue, W is blood perfusion and Q is the metabolic heat generation of the tissue. The last term represents the externally applied heat. A steady-state temperature distribution can give information about the predicted location of the hot spots in the brain and is given by solving the equation 3.2 for when the time-derivative is

set to zero.

The external heat source, or the power loss density (PLD), obtained from the optimal steering parameters can be tuned to reach a desired temperature [119]. Iterative scaling of the PLD can be done until a specified temperature is reached in the patient.

3.2.3 Treatment indicators

Treatment plans can be evaluated using quality indicators that are either SAR-based or temperature-based [2]. SAR-based quality indicators include HTQ, HCQ, and TC_x. HTQ and HCQ can also be used as cost functions during optimization [14]. The HTQ is defined as

$$\mathrm{HTQ} = \frac{\overline{\mathrm{SAR}}_{R1}}{\overline{\mathrm{SAR}}_{T}} \tag{3.3}$$

meaning the ratio between the average SAR in the volume of non-target tissues, $|R|$, with the highest 1-percentile SAR and the average SAR in the target volume $|T|$ [2]. However, the correlation between HTQ and high, homogeneous thermal tumor coverage is lacking [119]. Due to the definition of HTQ, part of the target volume can remain cold despite the HTQ value being low. HCQ was developed to address the disadvantages of HTQ.

HCQ suppresses the SAR peaks to avoid hot spots in the healthy tissue while covering the target tissue with sufficient energy deposition to gain a more uniform heat distribution [2]. The HCQ is defined as

$$\mathrm{HCQ}_p = \frac{\overline{\mathrm{SAR}}_{Rq}}{\overline{\mathrm{SAR}}_{Tp}} \tag{3.4}$$

where $\overline{\mathrm{SAR}_{Rq}}$ is the average SAR in the q-percentile of tissue outside of target tissue with the highest SAR, and $\overline{\mathrm{SAR}_{Tp}}$ is the average SAR in the p-percentile of the target tissue with the lowest SAR [2]. q and p are related to the target tissue volume, $|T|$, and the volume of the tissue outside the target, $|R|$, as $q = p|T|/|R|$.

There are also SAR-based indicators that can not be used as cost functions, like the iso-SAR target coverage TC_x which is only used as a quality indicator. TC_x is defined as the ratio between the target volume where SAR values are above a fraction x and the SAR peak value in the entire patient volume, $V_T(x)/V_T$. Direct correlation to clinical outcome has been observed for TC_{25} in the pelvic region [120], and for TC_{50} in the head and neck region [121].

Temperature-based quality indicators include T_{90} and T_{50}. T_{90} is a temperature distribution indicator that denotes the temperature exceeded by 90 % of the target volume [2]. Similarly, T_{50} denotes the median temperature in the target. Several clinical studies have shown that T_{90} directly relates to treatment outcome [122]. The median temperature has also been observed to have a relation to treatment outcome, although not as strong as the T_{90}.

Both T_{90} and T_{50} have been shown to correlate to the HTQ and HCQ to varying degrees [2]. The correlation between HTQ and T_{90} is relatively low [119]. In contrast,

the HCQ has demonstrated a stronger correlation to T_{90} with the HCQ producing higher T_{90} and T_{50} values when used as a cost function compared to HTC [119].

3.3 Applicator design

The quality of the hyperthermia treatment depends not only on the treatment plan itself but also on the design of the applicator. Important factors to consider for applicator design include the operating frequency, antenna types, the number of antennas, and the array design [2]. The target size and location are thought to impact the optimal applicator design.

Currently, there is no clear consensus on the optimal operating frequency, the optimal number of antennas, or what the optimal array design is for tumors in delicate areas such as the head and neck or brain. Paulides et al. (2005) found that a ring-array with 8 antennas was most suitable for head and neck tumors and that the optimal frequency was between 400-600 MHz depending on the target volume [123]. Guèrin et al. (2017) conclude that 900 MHz yields the highest ultimate SAR amplification factor (uSAF) [124]. Takook et al. (2018) found that an optimal brain applicator should include over 20 antennas that operate at different frequencies [125]. Oberacker et al. (2020, 2021) conceptualized RF applicators operating at 298 MHz that target glioblastoma multiforme [126] and found a 16-channel two-row arrangement to be most optimal [127]. Redr et al. (2022) demonstrated that a 12-antenna array operating at 434 MHz was the best candidate for hyperthermia treatment of brain tumors [128]. In the pelvic region, optimal frequencies for hyperthermia generally are 200-500 MHz [129], [130], [131].

The limitation of all mentioned studies is a parametric optimization process, meaning the optimization has been based on a fixed set of parameters such as a set of frequencies or a number of antennas. This does not account for potential non-linearity, particularly if the step-size is large, which could affect the results.

3.4 Array optimization

The T_{90} and T_{50} for a helmet applicator has been shown to improve with an optimized antenna array compared to a standard ring-array [132]. To obtain an optimized array, multiple simulations are necessary [132]. The process can be seen in figure 3.4 where the top row shows the three key elements used for simulations (patient, bolus and antennas) and the second row shows the simulations (electric field, coupling) that lead to the optimized array. First, the patient, antenna, and water bolus need to be modeled as in treatment planning. Afterward, simulations of single antenna fields and coupling are used for interpolation of the electric fields. Through field interpolation, the electromagnetic field distribution for any array configuration can be determined without the full simulation [132]. Approximating the fields by interpolation is much faster compared to doing a full simulation, making it possible to evaluate many arrays. Lastly, an optimization algorithm can be used to determine the optimal array for a given target.

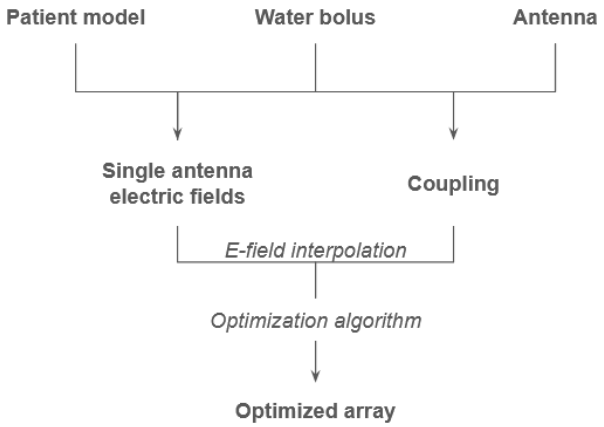

Figure 3.4: Overview of the design process to obtain an optimized array.

3.4.1 Electric field interpolation

The electric field interpolation is based on the fields of single antennas at different locations both on the bolus and the coupling between pairs of antennas at various distances [132].

Single antenna electric fields

To obtain the single antenna fields, the surface of the water bolus is divided into a uniformly distributed grid of n_p points [132]. The distance between two grid points should be no more than half of the minimum wavelength in water. The antenna's electric field in each grid point is then simulated for every frequency. After the simulations, the electric field from a single antenna a at any position $x_a, y_a, z_a = O_a$ on the bolus surface can be determined by linear interpolation. Figure 3.5 shows a grid with O_a marked in pink and the three grid points closest to a in solid grey.

The linear interpolation utilizes the fields E_1, E_2, E_3 of the three grid points closest to O_a [132]. Each field at frequency f is divided by the local impedance of the material, η_f, to reduce the field's dependency on the patient's anatomy. The divided fields are then transformed via translation and rotation such that the origin of E_i, $x_i, y_i, z_i = O_i$, is placed at O_a. Then, the transformed fields are multiplied with η_f, yielding the transformed electric fields $\hat{\mathrm{E}}_1, \hat{\mathrm{E}}_2, \hat{\mathrm{E}}_3$. The electric field of a is obtained from a weighted average of the transformed fields

$$E_a = \omega_1 \hat{\mathrm{E}}_1 + \omega_2 \hat{\mathrm{E}}_2 + \omega_3 \hat{\mathrm{E}}_3 \tag{3.5}$$

where ω_i denotes the weight [132]. Each weight is determined by the position of the grid points in relation to the antenna according to

$$\begin{aligned} \omega_1 &= \| (O_a, O_2, O_3) \| \; / \; \| (O_1, O_2, O_3) \| \\ \omega_2 &= \| (O_1, O_a, O_3) \| \; / \; \| (O_1, O_2, O_3) \| \\ \omega_3 &= \| (O_1, O_2, O_a) \| \; / \; \| (O_1, O_2, O_3) \| \end{aligned} \tag{3.6}$$

where $\| (O_a, O_2, O_3) \|$ is the triangular area between O_a and the second and third grid point, and $\| (O_1, O_2, O_3) \|$ is the triangular area between all grid points [132].

Now, the field from one antenna anywhere on the bolus surface can be determined. However, when an antenna in an array radiates, mutual coupling between antennas

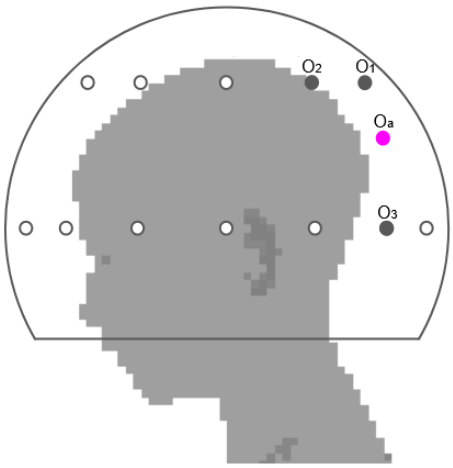

Figure 3.5: Patient model (grey) inside an outlined water bolus with grid points. An antenna location O_a is marked in pink, with the three closets grid points O_1, O_2, O_3 marked in solid grey.

occurs because the waves propagate not only through the patient but also through the water bolus, reaching the other antennas [2]. To estimate the field from an array of antennas, the coupling distortion of each antenna in the array also needs to be modeled [132].

Coupling detection

The coupling factor between two antennas in the bolus is determined by adding an active antenna A and a passive antenna P [132]. A is kept in a fixed spot, and a number of random locations are generated for P. First, the individual electric fields E_A and E_P are simulated for each arrangement of A and P. To obtain individual fields, only the antenna whose field is being simulated is present.

Secondly, the value of E_A at the phase center of the passive antenna, $E_A(O_P)$, is extracted. $E_A(O_P)$ is then projected onto the polarization axis of the passive antenna, U_P, by taking the scalar product between U_P and $E_A(O_P)$. This yields a scalar

$$e_{AP} = \langle U_P, E_A(O_P) \rangle \tag{3.7}$$

Third, the electric field from A when P is present, E_{A+P}, is simulated. Assuming both antennas are perfect electric conductors, the electric field becomes an infinite sum of reflections between A and P

$$E_{A+P} = E_A + k_{AP} \cdot (E_P + k_{PA} \cdot (E_A + k_{AP} \cdot (...))) \tag{3.8}$$

where $k_{AP} = k_{PA}$ is the coupling factor between A and P. However, due to domain losses, the overall field can be approximated as

$$E_{A+P} \approx E_A + k_{AP} \cdot E_P \tag{3.9}$$

e_{AP} and k_{AP} have been shown to have a linear relation which, for an arbitrary arrangement of A and P in a domain, can be described as

$$e_{AP} = c \cdot k_{AP} \tag{3.10}$$

where c is a complex coefficient [132].

Now, the electric field of each antenna in an array can be approximated as

$$\begin{bmatrix} \hat{E}_1 \\ \hat{E}_2 \\ \vdots \\ \hat{E}_n \end{bmatrix} = \begin{bmatrix} 1 & ce_{12} & \cdots & ce_{1n} \\ ce_{21} & 1 & \cdots & ce_{2n} \\ \vdots & \vdots & \ddots & \vdots \\ ce_{n1} & ce_{n2} & \cdots & 1 \end{bmatrix}^2 \begin{bmatrix} E_1 \\ E_2 \\ \vdots \\ E_n \end{bmatrix} \tag{3.11}$$

where n is the total number of antennas in the array [132].

3.4.2 Optimization algorithm

An optimization algorithm that finds the optimal array for a given target and a set number of antennas has been proposed in [132]. The algorithm evaluates thousands of possible arrays to find the optimal one, a task that could not have been completed in a feasible time frame by full simulations of every array.

The optimization algorithm is based on a random search (RS) strategy, followed by local refinement (LR) [132]. Figure 3.6a shows an overview of the optimization algorithm with the two stages. In the RS stage, a number of random, uniformly distributed arrays are generated. All arrays are evaluated based on HCQ, and then locally refined in order of ascending HCQ. In the LR stage, the array is refined using the nonlinear optimization function `fmincon` from MATLAB. The minimum HCQ for the first optimized array is determined, followed by the next array until the HCQ becomes worse.

Evaluation of the HCQ is done by utilizing the approximated antenna fields obtained from interpolation [132]. This process can be seen in figure 3.6b, and is repeated every time the array is evaluated throughout the optimization process. The steering parameters for each antenna are determined using i-TR. Then, the treatment plan is evaluated by determining the HCQ.

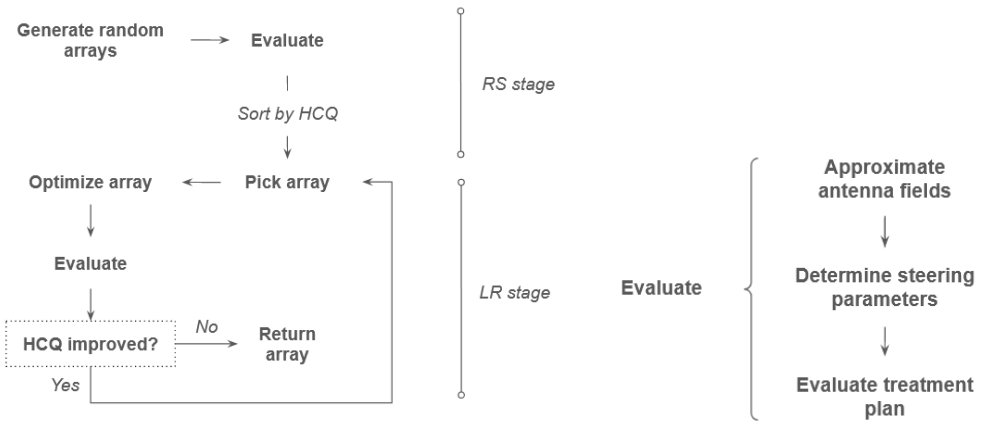

(a) Optimization process **(b)** Inner loop

Figure 3.6: Visualization of the optimization algorithm with (a) the overall process and (b) the inner loop used for evaluation.

4

Method

In this project, the first step was a literature review on pediatric brain tumors to find targets that could benefit from hyperthermia treatment. Afterward, simulations were done for two study cases. Study case one investigated the effects of target size, shape, location, and tissue properties on the temperature distribution and the optimal operating frequencies. The second study case used two different antenna arrangements within the applicator to study the effect of the array on the optimal operating frequency.

4.1 Literature review

The literature review was used to find data on histology, epidemiology, incidence rate, and relative survival rate for pediatric brain tumors. Then, information regarding the age and tumor size was obtained from population-based studies. The literature review used databases such as PubMed, Google Scholar, and the Institute of Electrical and Electronics Engineers (IEEE) Explore with articles written in English. Search terms are listed in table 4.1 with their respective database.

The data collected for this project was based on population-based studies, most of which involve pediatric patients in the age range of $0 - 14$. However, due to the rarity of specific pediatric brain tumors, a few studies with a larger age group using the keyword "pediatric patients" were included. If data on patient age and tumor size was available, the age limit was set to $0 - 14$ years with a recalculation of the mean size. The data was gathered from the statistical report $(2016 - 2021)$ by CBTRUS, a database focused on primary brain and other central nervous system (CNS) tumors in the United States.

4.2 Numerical simulations

The simulations followed the workflow of the treatment planning, as described in section 3.2. First, SAR-based treatment planning was done using i-TR and HCQ to obtain the optimal antenna steering parameters. Then, steady-state thermal simulations were done to evaluate the resulting temperature distribution using T_{90}. A constraint to not exceed 43 °C in healthy tissue was used when scaling the PLD.

COMSOL Multiphysics® 6.1 with LiveLink™ for MATLAB® was used for both the electromagnetic and thermal simulations. Tetrahedral mesh with a resolution of 5 elements per wavelength was used for the background air and water bolus. The total amount of domain elements was aimed to be less than 600,000 to limit the computational load.

During thermal simulations, heat flux boundary conditions were added to model thermal exchange at material interfaces. The convection coefficient between skin and

Table 4.1: Databases with dates and specific search terms. Note that *tumor* refers to replacing the search term with different types of brain tumors.

Database	Timeline	Keywords
Google Scholar	17 Jan-20 June	pediatric brain tumors, pediatric *tumor* histology, hyperthermia pediatric cancer, data and statistics on pediatric *tumor*, difference between adult and pediatric tumors, histology PBT, distribution of *tumor* location, PBT size and location, treatment pediatric brain *tumor*, management for pediatric *tumor*, population-based study of *tumor*, common location of pediatric brain *tumor*, treatment for pediatric *tumor*, current treatment *tumor*, statistics for children brain tumors, mean pediatric *tumor* size, *tumor* size in cm, *tumor* size in volume WHO grade *tumor*, WHO classification of glioma, WHO classification 2021, classification of brain tumors, classification of pediatric brain tumors, prognostic factors for pediatric brain tumors, common symptoms in pediatric brain *tumor*, anatomy of the brain, different function of brain regions, factors improving patient outcome for PBT, clinical features of *tumor*, long-term side-effects of treatments for pediatric brain tumors,
PubMed	17 Jan-30 Mar	brain tumors in children, malignant pediatric tumors, childhood brain tumors, incidence and survival rate of childhood brain tumors, data on pediatric brain tumors, *tumor* in children, case studies PBT, treatment of pediatric *tumor*, relative survival rate and incidence rate PBT
IEEE Explore	17 Jan-30 Mar	epidemiology of *tumor* in children, histology and location of *tumor* in children, population-based studies on pediatric *tumor*

air was $h_{s,a} = 8$ $\mathrm{Wm^{-2}K^{-1}}$, and between skin and water $h_{s,w} = 100$ $\mathrm{Wm^{-2}K^{-1}}$ [132]. Air and water temperatures were set to $T_{air} = 20$ °C and $T_{water} = 30$ °C respectively. The water temperature was set higher because some targets were superficial enough to be affected by the cooling from the bolus.

4.3 Frequency analysis

The analysis of optimal operating frequencies was carried out in the same band for single frequencies as well as frequency combinations. Eleven single frequencies between $250 - 800$ MHz, f=[250, 275, 300, 350, 400, 450, 500, 550, 600, 700, 800] MHz, were used to determine which frequencies contribute the most to the heat distribution indicator, T_{90}, in the treatment planning. Additionally, six combinations of frequencies between $250 - 550$ MHz, f=[250+350, 250+450, 250+550, 350+450, 350+550, 450+550], were used to study the effect of multiple frequencies.

4.4 Tissue properties

Four types of tissue with different tissue properties were used to analyze their effect on the T_{90}. The four types were

- **Healthy tissue**: the tissues in the target remained unchanged from healthy tissue. If the target overlapped with air, the air was omitted from the target volume.
- **Average tissue**: the tissue in the target was set to have the average properties of all tissues in the target volume.
- **Tumor (benchmark)**: the tissue in the target was set to tumor tissue using parameters from Joines et al. [133] and the European Society for Hyperthermic Oncology (ESHO) benchmark [3].
- **Tumor (Schooneveldt)**: the tissue in the target was set to tumor tissue using parameters from Joines et al. [133] and Schooneveldt et al. [4].

An overview of the parameters used for the average- and tumor-tissue targets can be seen in table 4.2. Target types named after a tumor represent the average tissue properties overlaying the tumor target volume.

Blood perfusion rate, specific heat capacity, and thermal conductivity were all thought to impact the resulting temperature distribution. A lower blood perfusion rate leads to lower blood flow and lower heat dissipation in the tissues, resulting in an uneven heat distribution. As the tumor (Schooneveldt) has the lowest perfusion rate, the heat should be the most retained in that tumor tissue. With a higher specific heat capacity, more energy, and thus a longer time, is needed to raise the temperature, but the target will in turn retain the heat better and maintain the temperature for a longer time. A higher thermal conductivity results in a faster heat transfer. When the target volume covering the tumor is heated, the tumor tissue would act as a good heat sink which potentially leads to a more uniform heat distribution. On the other hand, it is more difficult to achieve a high temperature within the tumor itself as the heat might dissipate to nearby healthy tissues.

Table 4.2: Dielectric and thermal tissue properties for homogeneous hyperthermia targets at 500 MHz: electrical conductivity, σ, relative permittivity, ε_r, mass density, ρ, specific heat capacity, c_p, thermal conductivity, κ, and blood perfusion rate, Q. Properties for craniopharyngioma, DMG, ependymoma, meningioma, and skull base were averaged based on the healthy tissue parameters from the IT'IS database [134].

Type	σ [S/m]	ε_r [-]	ρ [kg/m^3]	c_p [J/(kgK)]	κ [W/(mK)]	Q [1/s]
Craniopharyngioma	0.87	44.90	1027	3166	0.45	0.0124
DMG	1.34	56.95	1053	3701	0.52	0.0084
Ependymoma	0.71	48.54	1039	3661	0.51	0.0069
Meningioma	0.82	51.45	1039	3694	0.52	0.0079
Skull base	0.84	44.36	1122	3307	0.46	0.0070
Tumor (benchmark)	0.92[a]	58.67[a]	1090[b]	3421[b]	0.49[b]	0.0017[b]
Tumor (Schooneveldt)	0.92[a]	58.67[a]	1056[c]	3700[c]	0.57[c]	5.9E-6[c]

[a] average from Joines et al. [133] in accordance with the ESHO benchmark
[b] ESHO benchmark by Paulides et al. [3]
[c] Schooneveldt et al. [4]

4.5 Study case 1: Target characteristics and tissue properties

Study case one explored the effect of target size, shape, location, and tissue properties. The patient model used was Billie, an 11-year-old healthy female from the IT'IS Foundation [135]. Figure 4.1a shows the model of Billie's head where each color corresponds to a specific tissue. For full color key, see table A.1 in Appendix. The model had been optimized for finite-element modeling and featured 22 tissue groups divided into around 50 materials. All healthy tissue properties were obtained from the IT'IS Foundation database [134]. To limit the computational load whilst maintaining detail, a resolution of 5 mm was used. Similarly, only the head and shoulders of Billie were used, as the wave propagation beyond the shoulders was considered insignificant.

Figure 4.1b shows the patient model together with the bolus. The water bolus was modeled to be spherical with a radius of 14.39 cm. The bolus fit around the head of the patient and allowed the antennas to be placed a few centimeters from the skin. As seen in figure 4.1b, the bolus was cut off above the mouth to allow for breathing, and the cooling from the bolus was modeled to reach 2 cm deep into the model surface.

Next, tumor types and locations to be used as targets in the patient model were identified. First, the brain was divided into three regions: cerebrum, pituitary region, and posterior fossa. Then, the histologic subtypes of pediatric brain tumors, as reported by CBTRUS, were categorized into one of the three regions based on their common locations. Next, the incidence and relative survival rates were taken into consideration. The following were excluded:

- data from population-based studies that do not state tumor mean or median size

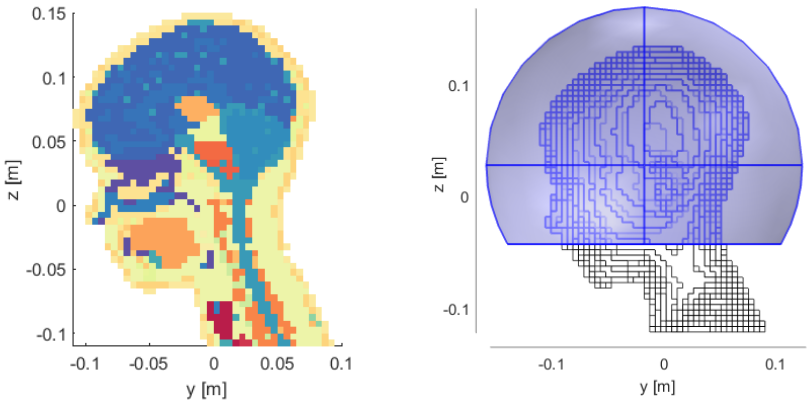

(a) Median sagittal section **(b)** Model and bolus surface

Figure 4.1: ZY view of the patient model with (a) differently colored tissue groups, see appendix table A.1, and (b) water bolus (blue).

- pediatric brain tumors commonly seen in the age group below the age of 4
- extracranial and spinal cord tumors
- overlap in common location of the chosen tumors
- tumors that receive craniospinal radiation as treatment

Through the literature study and contact with clinicians to confirm the anatomical location, four tumor types were chosen to model pediatric brain cancer. These included craniopharyngioma, diffuse midline glioma (H2K27M), ependymoma, and meningioma, seen in figure 4.2a-d. As the cerebrum is a large part of the brain, both meningioma and ependymoma were considered. Additionally, a smaller target volume of ependymoma was used to further analyze if tumor size affects the optimal frequency. See figure 4.2d-e for comparison. The targets were simplified and shaped as a full sphere with an exception for meningioma. Meningioma is commonly a superficial tumor and therefore the target was truncated at the skull to mimic a more realistic target for treatment. Other than the tumors from the literature study, a model of a skull base tumor from the Biomedical Electromagnetics group with an irregular shape was chosen to study the effect of tumor shape, seen in figure 4.2f.

All four tissue property types, healthy tissue, average tissue, and the two tumor tissues, were used for all targets. The only exception was the small ependymoma where only healthy tissue was used. Table 4.3 state the target volumes. Only craniopharyngioma had air overlaying the healthy tissues. The air was omitted with a resulting target volume of 22 ml, which is slightly lower than the 22.375 ml volume for the homogeneous targets that used either average or tumor tissue.

A self-grounded bow-tie (SGBT) antenna was used to model the array elements, shown in figure 4.3a. COMSOL Multiphysics® was used to calculate the antenna reflection coefficient between $250 - 600$ MHz with a step size of 50 MHz, shown in figure 4.3b. As seen in the figure, the S11 was below -10 dB across frequencies between $250 - 525$ MHz but increased for frequencies above 525 MHz. The antenna surface was modeled as a perfect electrical conductor (PEC) with a polarization axis aligned with the x-axis. A transverse electromagnetic (TEM) port with an impedance of 21.35 Ω was used to excite the antenna. Perfectly matched layers

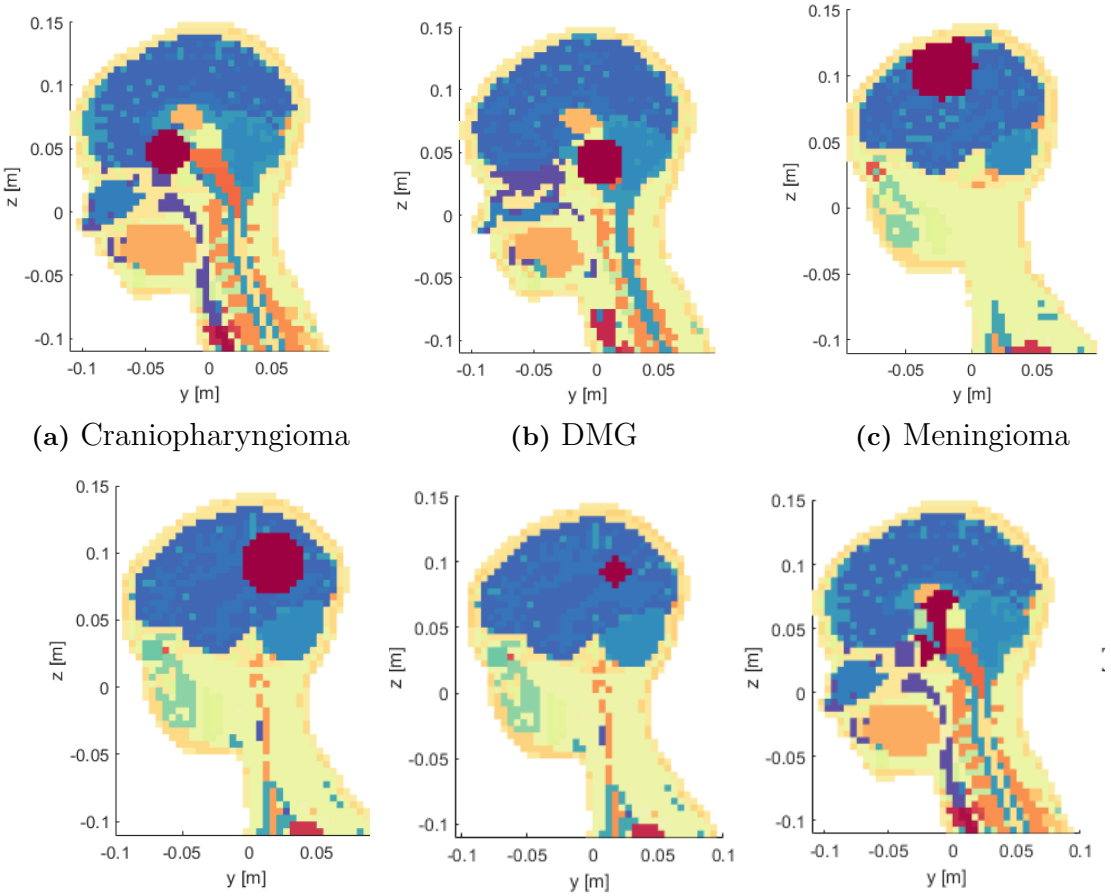

(a) Craniopharyngioma **(b)** DMG **(c)** Meningioma

(d) Ependymoma **(e)** Ependymoma (small) **(f)** Skull base

Figure 4.2: The sagittal section at the center of the tumor types (a)-(f), depicted as a red sphere in their respective size and location. Full tissue color key in appendix table A.1. (a) lies above sella turcica region, (b) in the pons, brainstem, (c) located on the left side of the cerebrum, (d)-(e) lying adjacent to the edge of the skull on the right cerebral hemisphere with different target size and (e) at the center of the brain.

Table 4.3: Target volumes for craniopharyngioma, DMG, ependymoma, meningioma, and skull base tumor.

Target type	volume [ml]
Craniopharyngioma (no air)	22
Craniopharyngioma	22.375
DMG	31.375
Ependymoma	48.625
Ependymoma (small)	7.125
Meningioma	55
Skull base	11.5

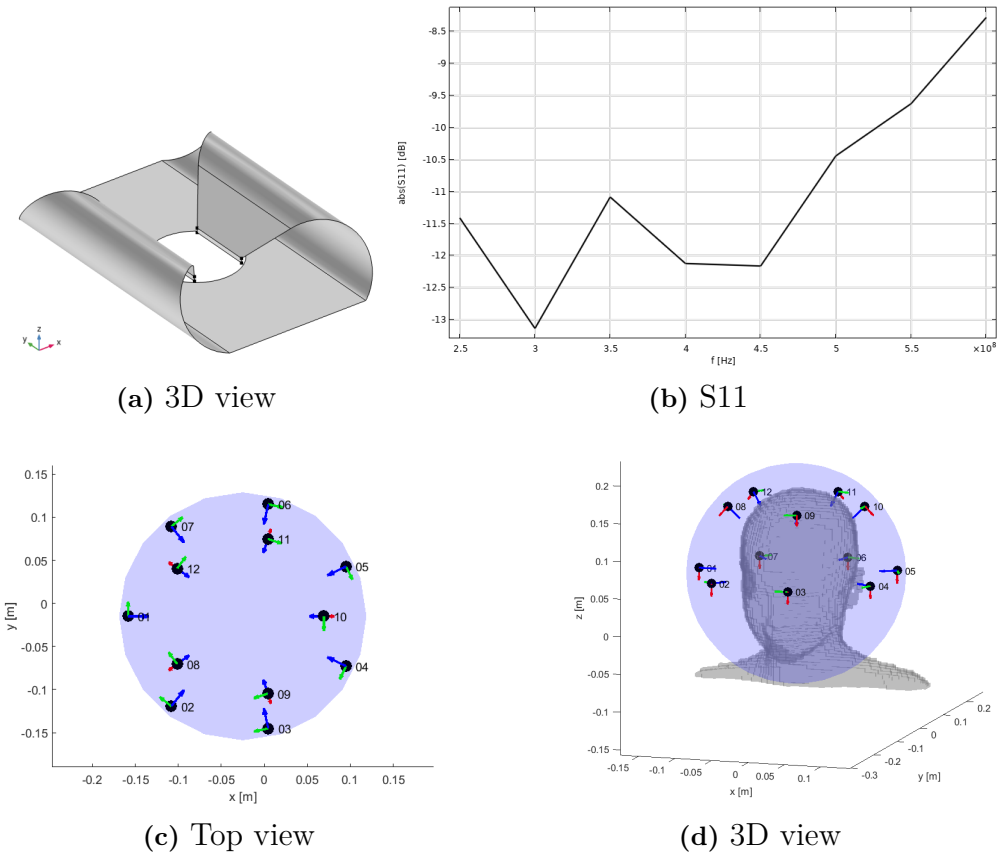

(a) 3D view **(b)** S11

(c) Top view **(d)** 3D view

Figure 4.3: Optimized SGBT (a) antenna geometry and (b) reflection coefficient in dB for frequencies between $250 - 600$ MHz. The antenna array configuration is shown with numbered array elements (black dots) on the bolus surface (blue) in (c) alone, and in (d) as used with the model. Note that the bolus is shown here as a full sphere to visualize the array.

(PML) defined absorbing conditions at the domain boundaries.

The treatment planning for all targets in study case 1 was done using a 12-antenna array with two rings of 6 antennas each, shown in figure 4.3c-d. As seen in figure 4.3d, antennae two and three were placed in front of the eyes. To avoid microwave radiation to the eyes, given their sensitivity, those two antennas were turned off.

4.6 Study case 2: Antenna arrays

Study case 2 investigated the effect of the antenna arrangement within the applicator. The patient model was a 13-year-old male with a medulloblastoma (126 ml) located in the dorsal region of the brain that had previously been used by Zanoli et al. [132]. Figure 4.4a shows the patient model with the medulloblastoma in orange. Full tissue color key is available in table A.2 in the Appendix. The model was based on 1 mm resolution segmented MRI data that had been up-sampled to a 4 mm resolution and featured 10 tissue groups [2]. Healthy tissue parameters were retrieved from the IT'IS database [134] and tumor tissue parameters followed the ESHO benchmark [3], stated as Tumor (benchmark) in table 4.2.

The water bolus had an ellipsoid shape with a radius of 12.5 cm along the x-axis, 14.2 cm along the y-axis, and 14.4 cm along the z-axis. It was cut off right above the nose of the patient model for breathing. Figure 4.4b-c shows the patient model and water bolus. Cooling from the bolus was modeled to reach 2 cm into the body surface.

A slightly different SGBT antenna was used as array elements compared to case 1, as case 2 featured the same antenna that Zanoli et al. had previously used with the patient model [132]. The antenna geometry can be seen in figure 4.4d. Antenna dimensions were 8.7 cm along the x-axis, 6.2 cm along the y-axis, and 2.4 cm along the z-axis. Figure 4.4e shows the antenna S11. The antenna had a reflection coefficient below -10 dB at 250 MHz and between $425 - 750$ MHz. As in study case one, the antenna was modeled as a PEC with a TEM port and a polarization axis along the x-axis.

The treatment planning was done for two arrays, a symmetric and an optimized

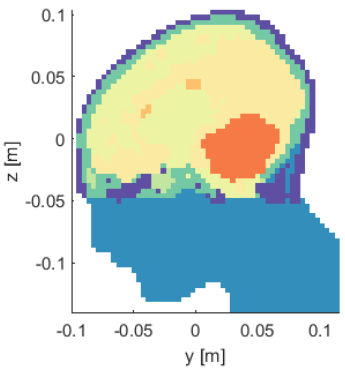

(a) Sagittal section at tumor center

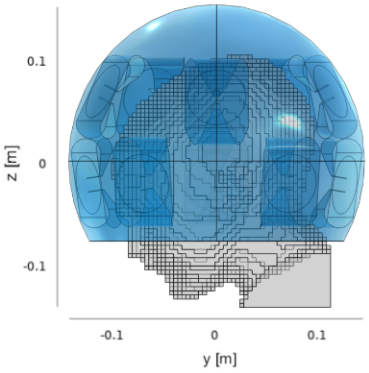

(b) Symmetric array

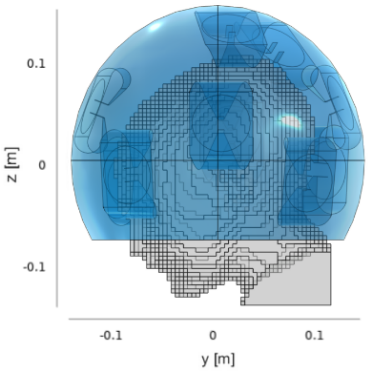

(c) Optimized array

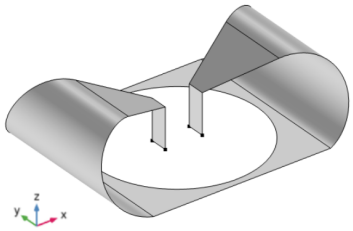

(d) 3D view

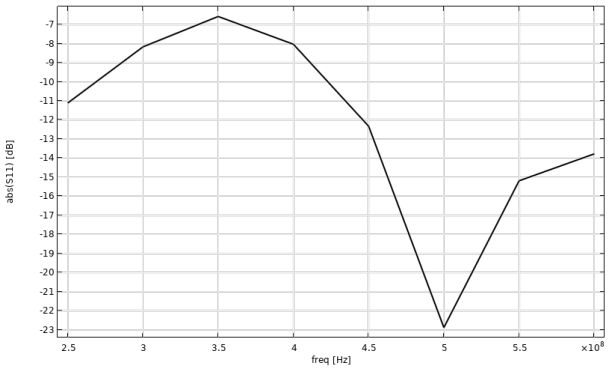

(e) S11

Figure 4.4: Elements used in study case 2. (a) show the patient model of a child with medulloblastoma (orange) and surrounding tissue, see table A.2 for full color key. Only the part above the head which covered the tumor and the applicator was segmented, the rest of the tissue was modeled as muscle. (b)-(c) shows the patient model (grey), water bolus (blue), and each array. (d)-(e) show the SGBT antenna geometry and reflection coefficient for frequencies between $250 - 600$ MHz.

array with 10 antennas, seen in figure 4.4b-c. These were chosen as the optimized array yielded the highest T_{90} in a previous study that compared symmetric and optimized arrays for a frequency combination of f = [250 375 500] MHz [132]. To protect the eyes, the second antenna was turned of when using the symmetric array. Both T_{90} and HCQ-values were used to evaluate the treatment plans.

5

Results

This chapter presents the results obtained for study case 1 followed by study case 2. The results of the frequency analysis using different tissue properties are illustrated for the various tumor types, according to Sec.4.4 and Sec.4.3. Any secondary results that may be relevant are reported in the Appendix.

5.1 Study case 1: Target characteristics and tissue properties

In the first case, the effects of target size, location, and tissue properties on the temperature distribution and the optimal operating frequencies were studied. Following the treatment planning workflow, the SAR distributions were obtained first, then the temperature maps and the T_{90}.

5.1.1 SAR distribution at the highest T_{90}

The two left columns in figure 5.1 show the normalized SAR distribution at the frequency and with the tissue properties that yielded the highest T_{90} for each target except the small ependymoma. All targets are outlined in white. Dark colors represent low energy absorption while light colors represent high absorption. The hot spot, the highest q-percentile outside of the target tissue, is shown in magenta, and the cold spot, the lowest p-percentile in the target, is shown in cyan. The top to bottom row shows craniopharyngioma at [350+450] MHz, DMG at 300 MHz, ependymoma at [250+350] MHz, meningioma at 275 MHz and skull base tumor at 300 MHz. All targets use tumor (Schooneveldt) tissue properties except meningioma which uses tumor (benchmark).

As can be seen in figure 5.1, DMG, ependymoma, meningioma, and skull base tumors have a lighter brown color in and around the target, which corresponds to an increase in absorbed energy. Meningioma shows energy absorption predominately in the target, with most of the healthy tissue being black or dark brown. Craniopharyngioma has a lighter color around the skull, but a relatively dark color in the target, corresponding to more energy being absorbed in the superficial, healthy tissues rather than in the tumor.

Hot spots appear close to the skin or around the target for DMG, ependymoma, meningioma, and skull base tumor, as indicated by magenta. For craniopharyngioma, the hot spot only appears close to the skin above the forehead. Cyan cold spots in craniopharyngioma, DMG, ependymoma, and skull base are generally located in the most deep-seated part of the tumor. On the contrary, the cold spots for meningioma is along the side of the target, closer to the skin.

5.1.2 Temperature distribution at the higest T_{90}

From the SAR distributions, the temperature distributions were obtained. Figure 5.1 shows the temperature distribution at the frequency and with the tissue properties that yielded the highest T_{90} for each target except the small ependymoma. The two right columns in figure 5.1 show the temperature maps that correspond to the SAR distributions on the two left columns. All targets are outlined in white. Dark blue represents tissue at 37 °C while dark red represents tissue around 43 °C. The black dot indicates the pixel that reached the highest temperature.

As seen in figure 5.1, the perimeter and the back of the patient are 37 °C for all targets. Craniopharyngioma has an area with elevated temperature close to the skull above the forehead, as indicated by the light blue to yellow color. Visible in the sagittal section, most of the healthy tissue from the eyes and to the jaw is heated to $39 - 42$ °C, indicated by the cyan to red color. The target is mostly red, corresponding to a temperature increase, but the heat is not uniformly distributed in the target. The highest temperature in the healthy tissue below the tumor is indicated by the black dot.

DMG has a higher temperature increase in the target, indicated by the dark red color in the tumor center, but the heat is not evenly distributed. Below the target, the area is cyan to red, meaning it is also heated. The area around the eyes and the optical nerve is blue, indicating little to no temperature increase there.

Ependymoma shows a dark red color in the entire target volume and a dark-colored area in the middle of the tumor, indicating a high, even temperature distribution with the highest temperature being the center of the tumor. A red-colored area can be seen at the back of the neck, indicating a hot spot. Between the target and the skin, and along the upper cheek, cyan indicates an increased temperature.

Meningioma also has a dark red color in the entire target volume, and a black dot in the center of the tumor, corresponding to a high, even temperature distribution. The healthy tissues are dark to light blue, indicating little temperature increase outside of the target.

The skull base tumor has a green-colored area above the forehead, and an area of cyan to red around the target, indicating hot areas in healthy tissue. A large area below the tumor is cyan to red, including the area of the eyes and the optical nerve. Most of the target volume is red to yellow, indicating an increased temperature but not a uniform temperature distribution.

Comparing the SAR distribution with the temperature distribution in figure 5.1, the SAR generally predicts the hot spots seen in the temperature distribution. However, there are exceptions, for craniopharyngioma and skull base, the SAR does not show the significant temperature increases that can be seen below the targets in the temperature map. Cold spots in the target are generally accurately predicted by the SAR distribution.

5.1.3 SAR and temperature maps at low frequencies

In the previous sections, the SAR and temperature map at the frequency and with the tissue properties that yielded the highest T_{90} for each target were shown. This section covers the typical SAR and temperature distribution for lower frequencies.

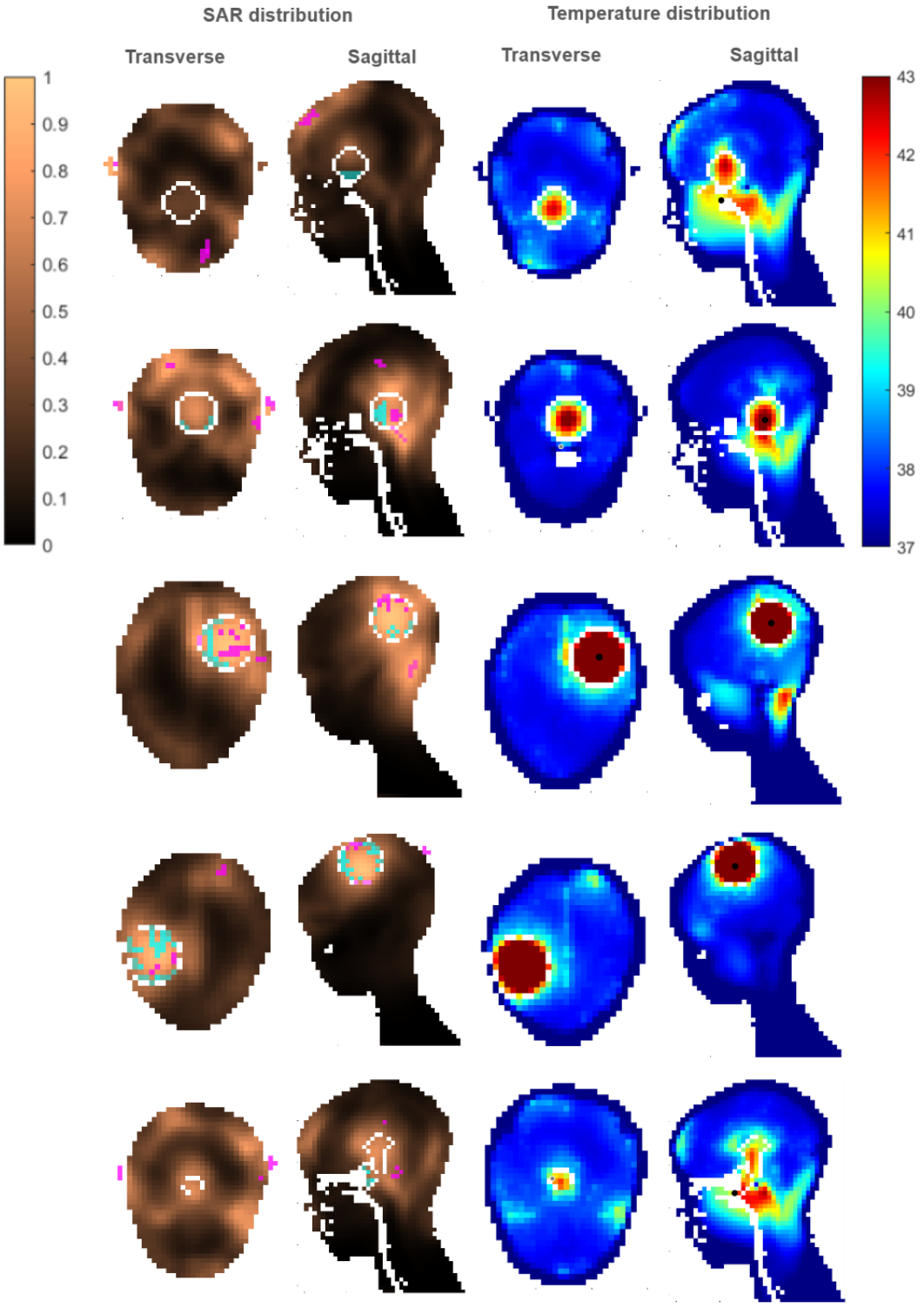

Figure 5.1: SAR and temperature distributions for the highest achieved T_{90} across all frequencies and target types. All use Schooneveldt properties except meningioma that use benchmark. Transverse and sagittal section at tumor center shown from the top: craniopharyngioma (350+450 MHz), DMG (300 MHz), ependymoma (250+350 MHz), meningioma (275 MHz), and skull base (300 MHz). Target is outlined in white. Magenta and cyan in the SAR maps represent hot spots and cold spots respectively. The black dot in the temperature maps represents the highest temperature.

Figure 5.2 presents the normalized SAR and the temperature distribution at 275 MHz for craniopharyngioma, DMG, ependymoma (original size), meningioma, and skull base targets using tumor (benchmark). As can be seen in the SAR distribution, areas in and around the target are lighter brown, indicating more energy absorption. Magenta hot spots are either by the skin or around the target. Cold spots, seen in cyan, are in the more deep-seated part of the target except for meningioma, where the cold spots are along the side of the tumor, emanating from the skull.

Looking at the temperature distributions, craniopharyngioma, DMG, and skull base tumors have cyan to red colored areas below the target, indicating heat increase in healthy tissue. The targets are cyan to red, corresponding to a temperature increase although not uniform. Ependymoma and meningioma have a high, even target temperature distribution seen as a dark red color. Ependymoma has an area of high temperature at the back of the neck and between the target and the skin, seen as cyan to yellow color. Healthy tissue around the meningioma is blue, corresponding to a little temperature increase.

The SAR and temperature distributions shown in figure 5.2 are similar for all frequencies between $250-350$ MHz and for frequency combinations between [250+350]-[350+450] MHz. Across all tissue types, SAR distribution was similar. Healthy and average tissue had less uniform thermal target coverage compared to the tumor tissues, but hot-spot locations were similar across tissue types. See appendix figure A.7 for SAR and temperature maps of ependymoma at 275 MHz for all tissue types. Differences in SAR and temperature maps between tumor (benchmark) and tumor (Schooneveldt) properties were minor.

5.1.4 SAR and temperature maps at high frequencies

After looking at a typical SAR and temperature map for lower frequencies, a similar figure is introduced for high frequencies. Figure 5.3 shows the normalized SAR distribution and the temperature distribution at 500 MHz for craniopharyngioma, DMG, ependymoma (original size), meningioma, and skull base targets using tumor (benchmark) properties. First looking at the SAR map, most of the patients are colored black to dark brown, corresponding to little to no energy absorption. The ependymoma target, the meningioma target, and the perimeter of all patients show a lighter brown color, indicating energy absorption. Magenta hot spots can be seen around the skin on top of the head.

Then looking at the temperature distribution, the craniopharyngioma, DMG, and skull base target are blue, corresponding to little to no temperature increase. Craniopharyngioma has cyan to red colored hot spots above the forehead, by the front of the face, and at the back of the neck. DMG also has a cyan to red hot spot at the back of the neck, whilst the skull base tumor has a cyan to green hot spot at the front of the face. Ependymoma and meningioma have green to dark red colored targets, indicating temperature increase but an uneven temperature distribution. They also have superficial hot spots around the skull, as seen in cyan to green and yellow.

Higher frequencies had similar SAR and temperature maps to figure 5.3. As for low frequencies, the SAR distribution was similar across tissue properties whilst the

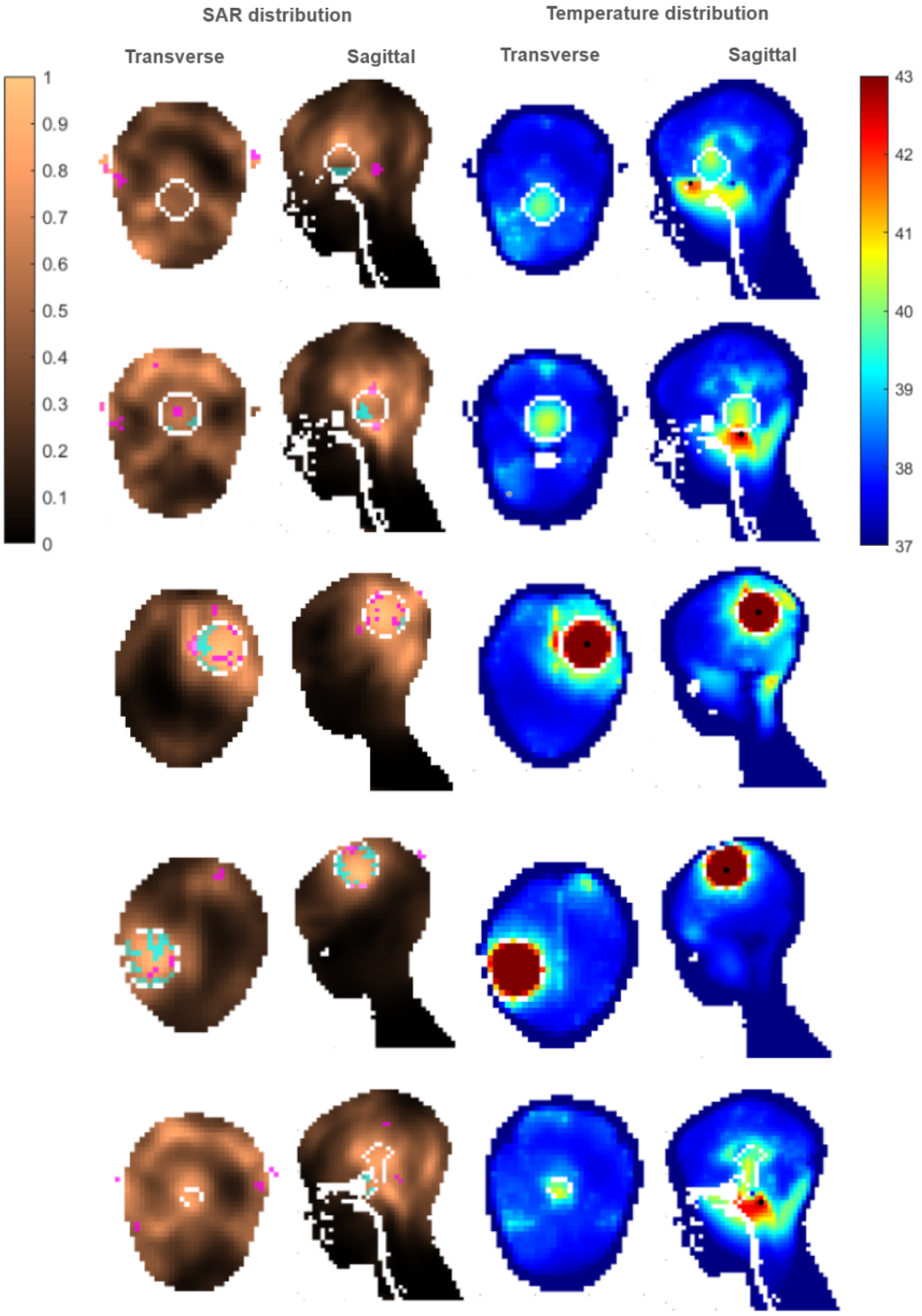

Figure 5.2: SAR and temperature distributions at 275 MHz with tumor tissue parameters from the ESHO benchmark, shown as transverse and sagittal section at tumor center for craniopharyngioma (top row), DMG, ependymoma, meningioma and skull base (bottom row). Target outlined in white. Magenta and cyan in the SAR maps represent hot spots and cold spots respectively. The black dot in the temperature maps represents the highest temperature.

temperature distribution for healthy and average tissue was less uniform than the tumor tissues. With increasing frequency, the tumor coverage steadily decreased and the superficial hot spots increased.

One important note is that the majority of hot spots occurred in the eye for craniopharyngioma even though the two antennas in front of the face were turned off. Thus, the results obtained are clinically irrelevant but the target will be discussed in terms of its shape, size, and location in the next chapter.

5.1.5 Target T_{90}

From the temperature distribution, the T_{90} could be determined. The T_{90} for each target and each tissue property is reported in figure 5.4. Frequency is shown on the x-axis and temperature on the y-axis. In figure 5.4a-c and e-f, the left, darkest bar, is the T_{90} using healthy tissue parameters. The second bar from the left shows the T_{90} using average tissue properties, followed by tumor (benchmark) properties, and the rightmost bar shows the T_{90} using tumor (Schooneveldt) properties. In figure 5.4e the T_{90} is shown as the darker, left bar for the originally sized ependymoma, and the as the lighter, right bar, for the smaller ependymoma, both using healthy tissue parameters.

The deep-seated targets achieved the lowest T_{90} values, particularly craniopharyngioma. Craniopharyngioma's highest achieved T_{90} was 39.6 °C using the frequency combination [250 + 350] MHz with tumor (Schooneveldt) properties, the lowest among all targets. DMG and skull base tumor achieved a highest T_{90} of 39.63 °C and 39.82 °C respectively, both at 300 MHz using tumor (Schooneveldt).

Ependymoma (original size) reached the highest T_{90} out of all tumors with a temperature of 43.04 °C using tumor (Schooneveldt) with the combination frequency [250 + 350] MHz. The smaller ependymoma reached at the highest T_{90} = 39.91 °C with frequency combination [250 + 450], which was similar to the highest T_{90} for ependymoma with healthy tissue, 39.85 °C at 275 MHz. Meningioma had the second highest T_{90} of 42.08 °C using tumor (benchmark) at 275 MHz.

Lower frequencies, between 250−350 MHz and [250+350]−[250+550] MHz achieved the highest T_{90} for targets, with all tissue properties. The higher frequencies seldom gave a high T_{90}, neither with the use of single frequencies or combinations of frequencies.

Deeper seated targets, craniopharyngioma, DMG, and skull base, had lower T_{90} across all tested frequencies compared to the more superficial targets ependymoma and meningioma. The deep-seated targets showed a relative increase in T_{90} at 600 MHz compared to surrounding frequencies, seen in figure 5.4a, b, and f. This could also be observed for the ependymoma at 500 MHz and the smaller ependymoma at 450 MHz.

Out of the four types of tissue properties, the parameters from tumor (Schooneveldt) presented the highest T_{90} in all tumors, with an exception for meningioma. The second highest achieved T_{90} was using parameters from tumor (benchmark), followed by average and healthy tissue parameters which were quite similar.

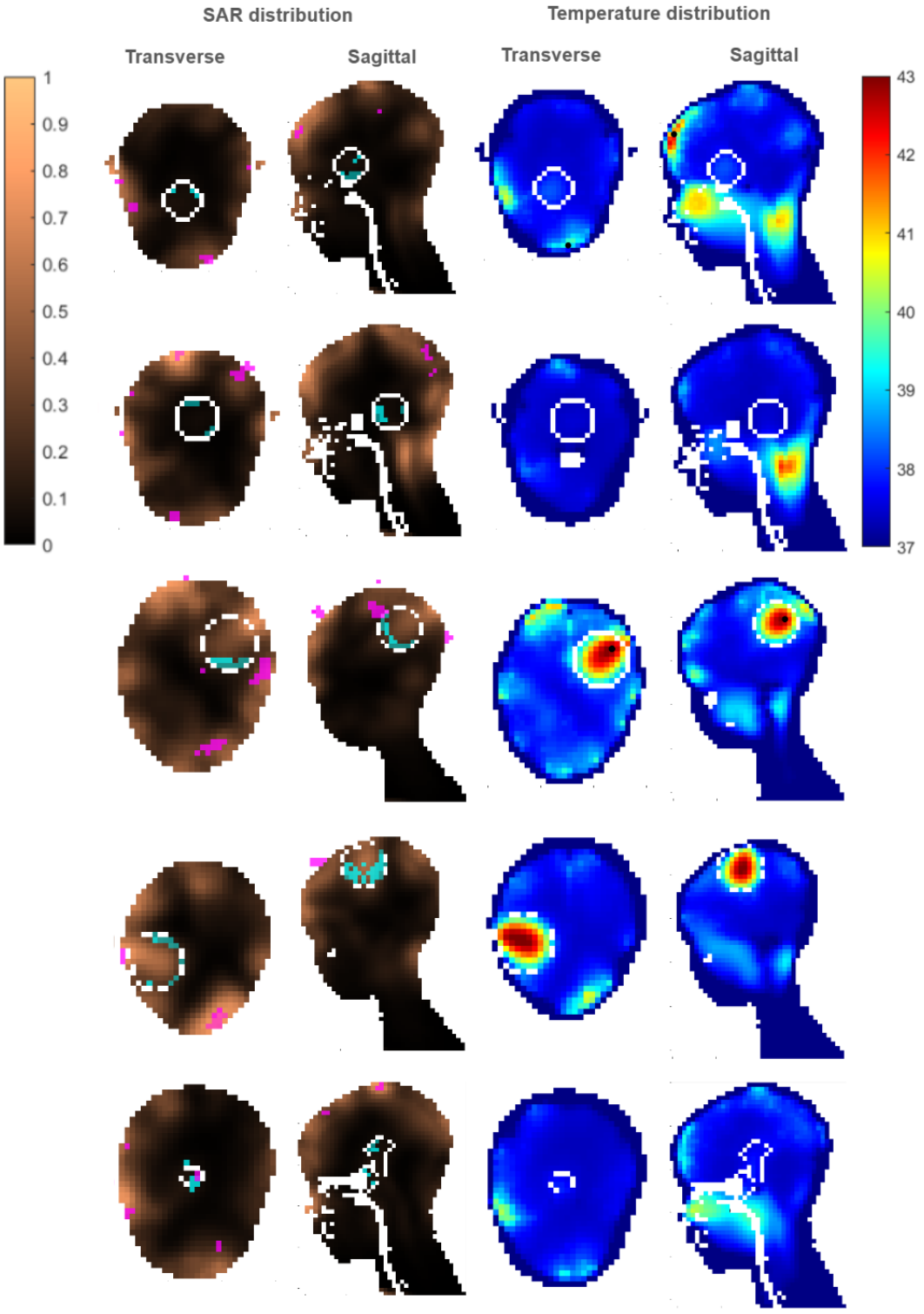

Figure 5.3: SAR and temperature distributions at 500 MHz with tumor tissue parameters from the ESHO benchmark, shown as transverse and sagittal section at tumor center for craniopharyngioma (top row), DMG, ependymoma, meningioma and skull base (bottom row). Target outlined in white. Magenta and cyan in the SAR maps represent hot spots and cold spots respectively. The black dot in the temperature maps represents the highest temperature.

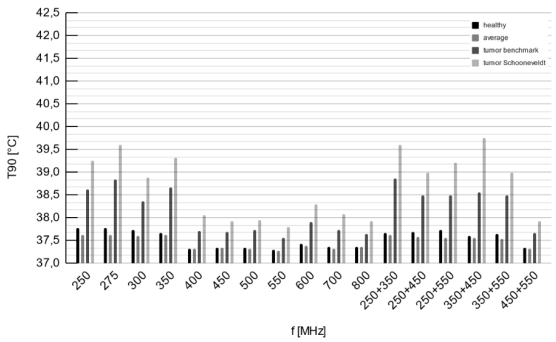

(a) Craniopharyngioma

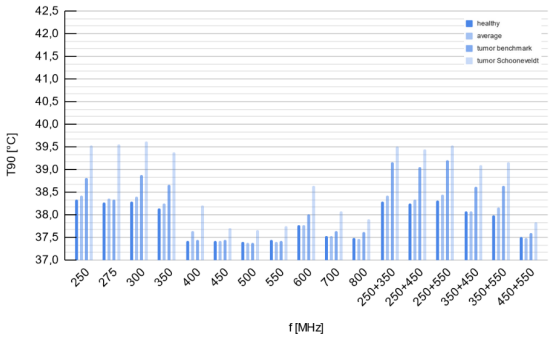

(b) DMG

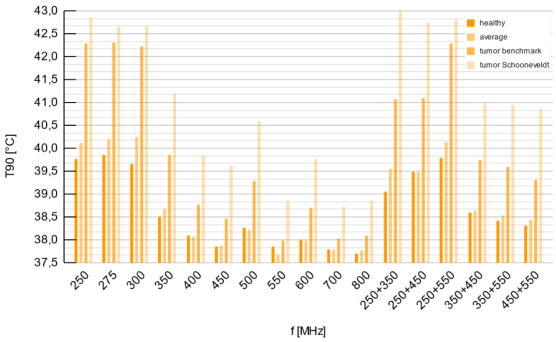

(c) Ependymoma (original)

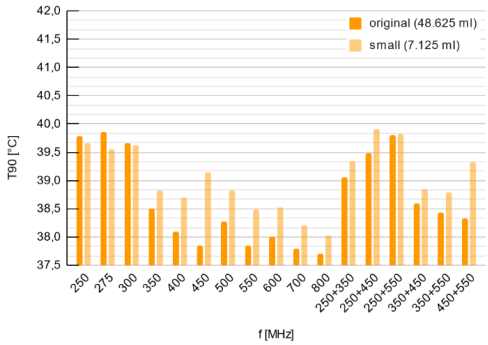

(d) Ependymoma

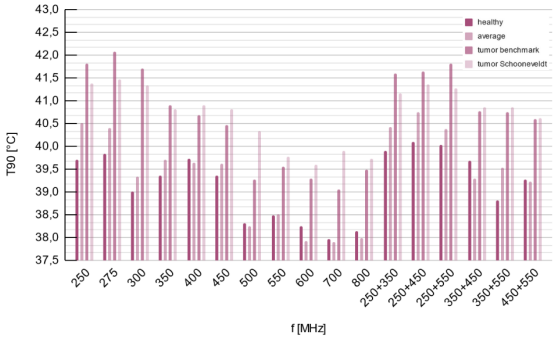

(e) Meningioma

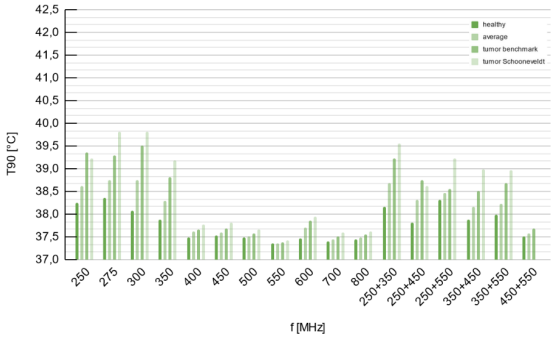

(f) Skull base

Figure 5.4: T_{90} at single frequencies and frequency combinations for each target. (d) show the T_{90} for healthy tissue parameters using the original (left bars) and smaller (right bars) ependymoma. Note that the y-axis runs between $37.0 - 42.5$ °C for (a)-(b), and between $37.5 - 43.0$ °C for (c)-(f).

5.2 Study case 2: Antenna arrays

Study case two featured a 13-year-old patient with medulloblastoma and used both a symmetric and an optimized antenna arrangement to investigate the effect of the array on the optimal operating frequency. The tumor tissue was modeled using tumor (benchmark) parameters.

5.2.1 SAR and temperature distributions

First, the SAR and temperature maps are introduced in figure 5.5. The normalized SAR distribution (left) and temperature distribution (right) for the symmetric array (two top rows) and the optimized array (two bottom rows) are shown at 275 MHz and 500 MHz. SAR and temperature distributions at lower and higher frequencies are similar to those shown at 275 MHz and 500 MHz respectively.

Looking at the SAR distributions at 275 MHz, both arrays show a similar energy distribution with lighter brown in and around the target and black to dark brown in healthy tissue. The symmetric array shows a lighter brown in the target and towards the back of the head, whilst the optimized array has a lighter-colored area on top of the forehead. Magenta hot spots are in similar locations in the transverse section, but the optimized array has a hot spot below the tumor in the sagittal section that the symmetric array does not have. The cyan cold spot in the symmetric array is toward the bottom of the target, and for the optimized array the cold spots are more at the sides of the target.

The SAR distribution at 500 MHz shows overall less absorbed energy for the symmetric array as the patient is mostly black, but higher absorption at the back of the neck in the sagittal section compared to the optimized array. Magenta hot spots are in similar locations, but the symmetric array shows a larger cold spot in the sagittal section compared to the optimized array.

Temperature distributions at each respective frequency are similar for both arrays, although not the same. At 275 MHz, the sagittal section shows a wider area of increased temperature below the target for the optimized array. Looking at the hot spot by the base of the neck at 500 MHz, it is cyan to yellow for the optimized array but cyan to dark red for the symmetric array. The temperature map of the symmetric array shows a more even thermal tumor coverage at 275 MHz and 500 MHz compared to the optimized array.

5.2.2 Target T_{90} and HCQ

After the distributions have been shown, the T_{90} and the HCQ cost across all tested frequencies for both the symmetric and the optimized array are shown in figure 5.6. Frequency is shown on the x-axis, temperature is read on the left y-axis, and HCQ cost is read on the right y-axis. The left, darkest colored bar, and the right, lighter colored bar show the T_{90} for the symmetric and optimal array respectively. HCQ values at each frequency are shown as a solid black line for the symmetric array and a dotted black line for the optimized array.

The highest T_{90} was 39.17 °C when using the symmetric array at 275 MHz.

Using the optimized array, the highest achieved T_{90} was 38.80 °C at 250 MHz. Similar temperatures, less than a degree from the maximum T_{90}, were reached for frequencies between 250 − 300 MHz and [250+350]−[250+550] MHz for both arrays. With increasing frequency, the T_{90} tends towards lower values, with the lowest T_{90} for both arrays being around 37.5 °C at 800 MHz.

For the lower frequencies that achieved the highest temperature, the difference between the arrays T_{90} is less than half a degree. Above 300 MHz, the optimized array has a higher T_{90} at a majority of the tested frequencies. The optimized array achieves half a degree or higher temperature than the symmetric array at 350 MHz, 550 MHz, and [350+550] MHz.

The lowest HCQ values were 1.523 and 1.421 at 250 MHz for the symmetric and optimized array respectively. With increasing frequency, the HCQ of both arrays trend upward. At lower frequencies, between 250−300 MHz and [250+350]−[250+550] MHz, the HCQ cost of both arrays is similar, with the optimized array being slightly lower. HCQ values were lower for the optimal array at all frequencies except at 450, 500, 700, 800, and [450+550] MHz.

HCQ and T_{90} follow each other with a lower cost at low frequencies where the T_{90} is high, and a higher cost at high frequencies where the T_{90} is lower. The HCQ is shown as a complement to the T_{90} because the array optimization is based on the estimated HCQ cost. Smaller discrepancies between T_{90} and HCQ exist; the HCQ for the symmetric array is higher at 275 MHz compared to at 250 or 300 MHz, but the T_{90} is the highest at 275 MHz.

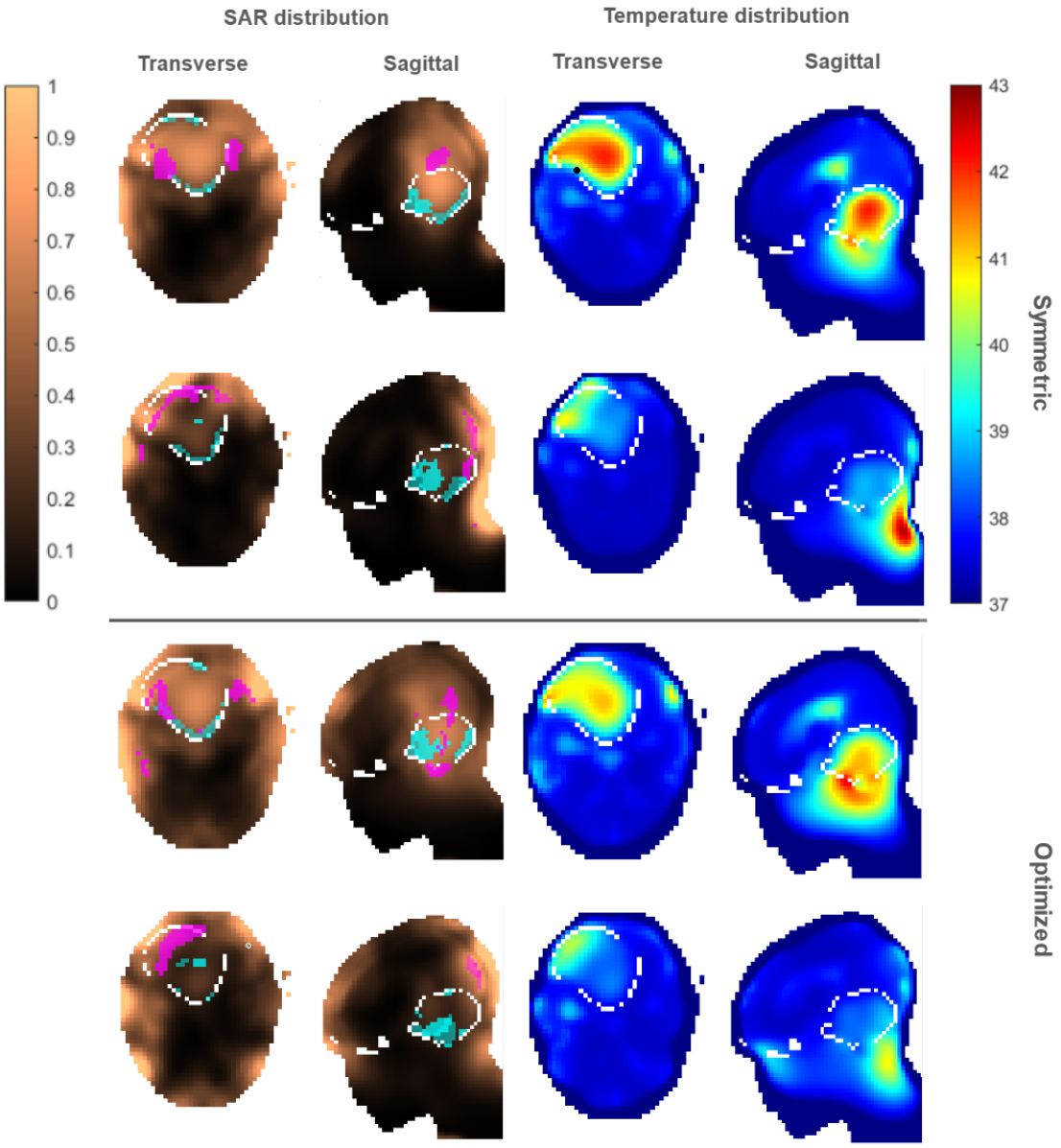

Figure 5.5: SAR and temperature distributions shown as transverse and sagittal section at tumor center. From the top: 275 MHz symmetric array, 500 MHz symmetric array, 275 MHz optimized array, 500 MHz optimized array. Target outlined in white. Magenta and cyan in the SAR maps represent hot spots and cold spots respectively. The black dot in the temperature maps represents the highest temperature.

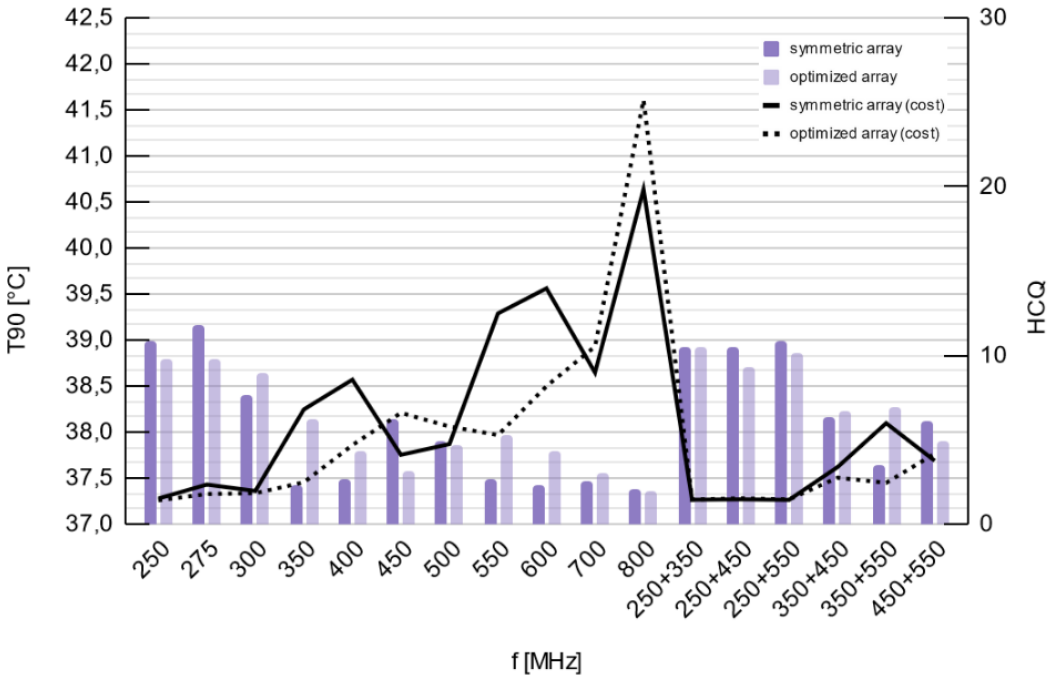

Figure 5.6: T_{90} at single frequencies and frequency combinations for the symmetric and optimized array with the respective HCQ value shown on the right axis.

6

Discussion

This chapter relates our findings to the aim and objectives. The targets are analyzed, followed by a discussion of the frequency analysis and the effect of target size, shape, location, and antenna arrays on the final temperature distribution. A comparison of our results and other available studies will be discussed at the end.

6.1 Literature study

From the literature review, we selected 4 tumor types: craniopharyngioma, DMG (formerly DIPG), ependymoma, and meningioma. These tumors were primarily chosen based on clinically relevant focal radiotherapy needs and due to their different spatial distributions across the brain. The size of the tumors was also selected based on available data. Both craniopharyngioma and DMG were investigated to assess if achieving therapeutically relevant temperatures is feasible, considering the complexity of the tumor location. Although most pediatric brain tumors occur in the cerebellum [32], we explored other locations, in particular meningioma and ependymoma. Other locations that could be explored, but were not due to time constraints, is the front of the cerebrum. These regions could be difficult to deliver heat even though it is a superficial tumor, as the region is in front of the head where the radiation to the eyes must be avoided.

The size of each tumor was obtained by population-based studies. In general, information regarding pediatric brain tumors was difficult to obtain since pediatric tumors have mostly been grouped with adult tumors. Furthermore, there was often a small sample size in most of the studies, sometimes only up to 10 patients. Even with available studies, the articles usually stated the tumor size range with a large variation, instead of the median or mean size. In the end, the mean tumor size could not be obtained for all the listed tumor types.

Although the tumors were of irregular shape, the study modeled them as perfect spherical targets to somehow represent a larger patient group. This carries a limitation of the analysis while evaluating the different factors. Therefore, a more realistic shape was later considered, that is the skull base tumor in case one and the medulloblastoma in case two.

The study was carried out in pediatric patient models of ages 11 and 13. This limited other tumors for the younger pediatric age group as the results will not be representative due to different head dimensions.

It should be noted that the age range for pediatric patients varies depending on the source. Some stated age $0 - 14$, others stated age $0 - 19$ and a few even considered age $20 - 21$ in the pediatric age group. This is understandable in terms of the little information available today about pediatric brain tumors. However, the

new classification from WHO 2021 of tumors in the brain and CNS made a step in the right direction by differentiating between pediatric and adult tumors.

6.2 Study case 1

The first study case aimed to investigate the effects of target size, location, and tissue properties on the temperature distribution and the optimal operating frequency. Out of all targets, only meningioma and ependymoma reached a T_{90} range of $40 - 43$ °C in the target volume. The smaller ependymoma achieved a higher T_{90} for f > 350 MHz compared to the original sized ependymoma, despite the center of each target being the same.

Our results indicate that single frequencies in the band of $250 - 350$ MHz as well as combinations of frequencies between $250 - 550$ MHz more effectively achieve both a higher temperature and a more uniform heat distribution in the target volume. Comparing the T_{90} as well as the SAR and temperature distributions between higher and lower frequencies, lower frequencies deliver a higher, homogeneous, thermal dose. As the frequencies increase the tumor coverage is reduced, resulting in lower T_{90} and hot spots appearing in superficial regions. For all tumor types, the T_{90} appeared to decrease at 350-400 MHz, and the low temperature was maintained or decreased at higher frequencies. Comparing the SAR distributions, more cold spots are present in the tumor volume at the higher frequencies compared to the lower frequencies. The temperature distribution at 275 MHz, seen in figure 5.2, presented hot spots either close to or inside the target volume for all tumors. At higher frequencies above 500 MHz, the temperature distribution shows the hot spots appearing at random superficial locations. The heat distribution in the target is also less uniform.

6.2.1 Tissue properties of targets

Focusing on the tissue properties, the targets in this study were artificially created by either keeping the original healthy tissue parameters, or by substituting the healthy tissue with average or tumor tissue parameters. For SAR calculations, the air was not taken into account by modification of the target. Therefore, a relevant question was to investigate the effect of the tumor properties on the resulting temperature distribution.

The main difference between the tested tissue parameters was a higher specific heat capacity, higher thermal conductivity, and a very low perfusion rate for tumor (Schooneveldt). Tumoral blood flow of adult gliomas has been determined to lie between $70.8-145.5$ (ml/100 g/min) [136]. This corresponds to around $0.0012-0.0254$ (1/s), suggesting that the tumor (benchmark) blood perfusion rate was more realistic than that of tumor (Schooneveldt).

Using tumor (Schooneveldt) resulted in the highest T_{90} of all tumor targets, except for meningioma. The lower T_{90} for meningioma using tumor (Schooneveldt) could depend on the target location, as it is a superficial target that lies directly beside the skull and is affected by the cooling effect of the bolus. As the cooling effect of the bolus reaches up to 2 cm into the skin, cooling of the target together with a higher thermal conductivity leads to the heat being conducted more easily, which

would reduce the temperature in the target volume.

In respect to the tumor types, the deep-seated targets, specifically craniopharyngioma and DMG, were the most challenging to achieve a high, homogeneous temperature distribution, regardless of tissue properties. When using average tissue, craniopharyngioma achieved lower T_{90} compared to all other tissue types, which was not the case for the other tumors where average tissue generally performed better than healthy tissue. The low T_{90} was probably due to the average tissue parameters of craniopharyngioma having the lowest specific heat capacity and thermal conductivity, combined with the highest perfusion rate compared to all other targets.

6.2.2 Target location, size, and shape

Looking at target characteristics, craniopharyngioma, DMG and skull base tumors were used to investigate the feasibility of heating deep-seated targets while ependymoma and meningioma were used to investigate the feasibility of heating superficial targets. The target depth was hypothesized to decrease the target temperature as the waves need to propagate further, as well as decrease the optimal operating frequency because the penetration depth of the wave decreases with higher frequencies. Both sizes of ependymoma were used to study different target volumes. A smaller target was thought to benefit from higher frequencies since the size of the spot decreased. The skull base tumor was used to study the effect of shape, as an irregular shape might benefit from frequency combinations that enable different-sized focal spots.

It is worth mentioning that direct comparison of these factors is difficult since the targets had unique properties and analyzing one factor individually proved to be difficult. Multiple characteristics varied between targets, such as the depth being affected when changing the size of the ependymoma. Nevertheless, frequencies between $250-350$ MHz had the highest T_{90} regardless of the size, shape, and location.

Regarding location, the deep-seated targets achieved a lower T_{90} across all frequencies and were more challenging to heat compared to the superficial targets. This can be seen from the SAR distributions for 500 MHz in figure 5.3. The highest SAR could be seen on the surface of the patient with the contours of the antenna, and the SAR decreases with depth, which leads to less energy deposition in the deeper tissues. As seen with craniopharyngioma, DMG, and skullbase, all three tumors achieved a similar T_{90} even with an irregular shape for the skull-base tumor. This indicates that location is a more significant factor than shape, but additional simulations are needed to confirm this conclusion. In terms of heat distribution, the deep-seated targets had a similar pattern where $250-350$ MHz achieved the highest T_{90} and then the temperature decreased with higher frequencies except for a sudden peak at 600 MHz.

All targets had different volumes, but we can see from figure 5.4 that the lower frequencies achieve a higher T_{90} for all targets. The lower frequencies also achieve the highest T_{90} for both of the different ependymomas, which further reinforces that lower frequencies achieve higher temperatures regardless of volume. Nevertheless, the target volume did seem to affect the temperature distribution for the frequencies

above 350 MHz. However, it could also depend on the location of the perimeter of the smaller ependymoma target, which lies deeper compared to the larger ependymoma. The center of both ependymomas was the same, but the difference in depth of their perimeter occurred due to their size variation.

Looking at the shape of the tumor types, the targets from the literature review were spherical while the skull base tumor had an irregular shape. The locations of the deep-seated tumors, DMG, craniopharyngioma, and skull base, were fairly similar, and the tumor volumes were on the lower end compared to meningioma and the large ependymoma. All three deep-seated targets had a similar T_{90} and followed the same pattern for the temperature distribution, despite the difference in tumor shape. The different tumor shapes did not give any noticeable difference, neither in terms of optimal frequencies nor in the final temperature distributions.

One important factor that would impact the index temperature like the T_{90}, is if the constraint for the highest temperature reached in the tissues was changed from 43 °C. Changing the maximum temperature constraint would impact the scaling factor applied after the thermal simulation. The therapeutic hyperthermia temperature range is $40 - 44$ °C, nevertheless, in a sensitive region such as the brain, thermal-related toxicity can already be presented at 42 °C. Therefore, the constraint should be lowered.

Other refinements for this study could involve using a finer step size for the frequency analysis to find out other frequencies at the lower end that can contribute more to the final temperature distribution in the target volume.

A continuation of this study would be to do additional simulations that systematically investigate target size, shape, and location. Location seems to be a bigger factor compared to size and shape. While the size and shape may have an impact on the final temperature distribution, we can not for certain state that one factor is more significant than the other without additional simulations to obtain a more accurate and definite conclusion.

6.3 Study case 2

Case 2 used a patient model, bolus, antenna and arrays that had previously been used by Zanoli et al. [132]. Single frequencies between $250 - 350$ MHz as well as [250+350]−[250+550] MHz had better T_{90} and HCQ values than higher frequencies, regardless of the array. These were the same frequencies that gave the highest T_{90} in case 1 as well. In case 1, the lower temperature at higher frequencies could be caused by poor performance of the antenna as the S11 only was below -10 dB for frequencies below 525 MHz. However, in case 2 the antenna S11 was below -10 dB at 250 MHz and in the frequency band of $425 - 750$ MHz. Despite different antenna characteristics, the same decrease in T_{90} for increased frequencies was found for all targets in both cases, suggesting that the results were not exclusively caused by the antenna performance.

The optimized array generally achieved higher T_{90} than the symmetric array. In particular, around the frequencies the array was optimized for, f = [250, 375, 500] MHz, the T_{90} and HCQ of the optimized array were similar or better than the symmetric array. Notably, the optimized array performs much better at 350 MHz,

550 MHz and [350+550] MHz. However, the symmetric array shows marginally higher T_{90} at 250 and 275 MHz. More data is necessary to draw a strong conclusion, but the results suggest that the optimization process is quite sensitive to the choice of frequencies.

Looking at the cost function's relation to the T_{90}, it generally follows the temperature well. However, for smaller temperature differences, the lowest HCQ value does not always correspond to the highest T_{90}. This is not unexpected as the SAR distribution does not have a linear correlation to the temperature distribution [2]. A consequence of this is that the optimal operating frequency might not be most accurately determined based on only the SAR distribution or a SAR-based indicator. This could also present a problem in the array optimization process because the arrays are evaluated based on their HCQ. The array that would yield the highest T_{90} might not be the final solution. A way to mitigate this could be to select the three or four frequencies or arrays with the lowest HCQ for thermal simulations before deciding the optimum. However, the inaccuracy in SAR due to interpolation would still be large.

Despite using the same treatment setup, optimization algorithms, and cost functions as Zanoli et al. [132], our temperature data is not directly comparable to the prior data. The most notable difference is the constraint to not exceed 43 °C during optimization after the thermal simulation, which was set to 42 °C by Zanoli. Electromagnetic simulation conditions were similar. One aspect that may differentiate the data is the use of a coarser mesh in this study.

An interesting progression of this work would be to optimize an array at the frequency or frequency combination that had the highest T_{90} for the canonical array. One way is to compare optimized arrays for some of the other targets used in case 1, such as ependymoma, DMG, or meningioma. Targets more centered inside the head, like DMG, could potentially benefit less from a non-symmetric array compared to targets like ependymoma which are offset from the center of the head.

6.4 Work in relation to literature

Looking at our results in relation to available literature, prior studies have explored optimal operating frequencies for microwave hyperthermia, but not in the same context as our work. The majority of studies were not carried out exclusively on pediatric brain tumors. A vast majority of studies considered adult patient models with targets located either in the pelvis or in the head and neck [123]-[131]. In contrast, this study only had targets in the different regions of the brain, and both cases used pediatric patients.

In this study, frequencies between $250-350$ MHz gave the highest T_{90} for all targets. This differs from previous studies where a majority found frequencies between $400-600$ MHz to be optimal for treating head and neck tumors. However, the frequency range in this study has not been considered previously. In particular, 250 or 275 MHz have not been explored for intracranial tumors. Several studies investigated the frequencies allocated to Industry, Science, and Medicine (ISM), 27.12, 434, and 2450 MHz in Europe and 27.12, 915, and 2450 MHz in the United States, as well as some additional frequencies [123], [128].

The portion of our data that is within a previously studied frequency range shows consistency with the literature, supporting the reliability of our results. Excluding frequencies between $250 - 350$ MHz and looking only at the T_{90} in the frequency range between $400 - 800$ MHz, our optimal operating frequency would be between $400 - 600$ MHz depending on the target, and the optimal ISM frequency would be 434 MHz. From figure 5.4, craniopharyngioma, DMG, and skull base achieve a maximum T_{90} at 600 MHz. The large and small ependymoma have a peak T_{90} at 500 MHz and 450 MHz respectively, and meningioma reach a maximum T_{90} at 400 MHz. Figure 5.6 shows a peak T_{90} at 450 MHz and 550 MHz for the symmetric and optimized array respectively. Thus, our data agree with previous studies when comparing the same frequencies.

One study has also proposed 900 MHz as the optimal frequency for head and neck tumors, but the study assessed the frequency performance based on the uSAF [124]. Maximizing the SAF is not the same as minimizing the HTQ, where the latter has been shown to have a better correlation to the thermal dose [14].

Other studies have suggested that a combination of frequencies, or UWB systems, could be optimal [2], [14], [125]. In this work, combinations of frequencies, particularly in the range of $250 - 550$ MHz, yielded similar T_{90} to the single frequencies in the $250 - 350$ MHz range. Hot spots in the temperature distribution for each target were in similar locations at frequency combinations with $250 - 500$ MHz and single frequencies between $250 - 350$ MHz. In case 2, the hot spots were in similar locations for both arrays. However, looking at the temperature maps for higher single frequencies, such as 500 MHz, the hot-spot intensity and location vary compared to lower frequencies. Although the T_{90} for frequencies > 350 MHz is lower, these frequencies could still be relevant in a clinical setting. As suggested in the literature, a UWB system that can change between two frequencies could allow for effective hot-spot suppression to limit patient discomfort. Based on our results, such a system would ideally be able to operate in the $250 - 350$ MHz range for maximum T_{90}, and in the $400 - 600$ MHz range for the alternate frequency. As different targets have different optimal operating frequencies in the $400 - 600$ MHz range, the best dual-frequency treatment plan should include the best low and high frequency for the specific target to allow for the highest thermal dose.

7

Conclusion

This study investigated the feasibility of external microwave hyperthermia for pediatric intracranial targets. A literature review and contact with clinicians identified four tumors to assess the accessibility of microwave heating based on target size and anatomical location: craniopharyngioma ($\approx$ 22 ml), DMG (H2K27M) ($\approx$ 31 ml), ependymoma ($\approx$ 49 ml) and meningioma (55 ml). A smaller ependymoma ($\approx$ 7 ml) and a skull base tumor ($\approx$ 11.5) were also investigated. First, SAR-based treatment planning using i-TR and HCQ, followed by thermal simulations, was done for each tumor at frequencies between $250-800$ MHz to asses the target characteristics (size, shape, location) and tissue properties' effect on both the final temperature distribution and the optimal operating frequency. Four different tissue types were used for each target: healthy tissue, average tissue, tumor (benchmark) tissue, and tumor (Schooneveldt) tissue. Second, the simulations were performed for a medulloblastoma (126 ml) with tumor (benchmark) tissue using both a symmetric array and an optimized array to assess the effect of two different antenna arrangements within a helmet applicator on the optimal operating frequency.

Superficial tumors appeared more accessible for microwave heating compared to deep-seated tumors as only the meningioma and ependymoma reached a therapeutically relevant temperature within the range of $40-43$ °C. Higher T_{90} was achieved for superficial tumors, and generally also when using tumor tissue parameters with lower perfusion. Target size and shape appeared to have a smaller impact on the target temperature distribution. Single frequencies between $250-350$ MHz and combinations of frequencies using $250-550$ MHz achieved the highest T_{90} for all targets, regardless of size, shape, location, and antenna array. Lower frequencies were also more effective in achieving a uniform heat distribution. However, as we used several tumors with different characteristics, it was difficult to reliably assess only one property at a time. To clearly determine the effect of each target property, further simulations that isolate one aspect at a time are necessary. A continuation of this work would be to explore arrays optimized for frequencies between $250-350$ MHz and study the effect of an optimized array on different target locations.

Bibliography

[1] National Cancer Institute. "Cancer statistics." (2020), [Online]. Available: https://www.cancer.gov/about-cancer/understanding/statistics. (Retrieved: 2024-04-05).

[2] M. Zanoli, "Ultra wideband microwave hyperthermia for brain cancer treatment," Ph.D. dissertation, Chalmers University of Technology, 2022.

[3] M. M. Paulides, D. B. Rodrigues, G. G. Bellizzi, *et al.*, "Esho benchmarks for computational modeling and optimization in hyperthermia therapy," *International Journal of Hyperthermia*, vol. 38, no. 1, pp. 1425–1442, 2021. DOI: 10.1080/02656736.2021.1979254.

[4] G. Schooneveldt, H. D. Trefná, M. Persson, *et al.*, "Hyperthermia treatment planning including convective flow in cerebrospinal fluid for brain tumour hyperthermia treatment using a novel dedicated paediatric brain applicator," *International Journal of Hyperthermia*, vol. 11, no. 8, p. 1183, 2019. DOI: 10.3390/cancers11081183.

[5] Cancer Research UK. "Cancer survival statistics." (2023), [Online]. Available: https://www.cancerresearchuk.org/health-professional/cancer-statistics/survival#heading-One. (Retrieved: 2023-06-16).

[6] Cancer Research UK. "Brain, other cns and intracranial tumours statistics." (2023), [Online]. Available: https://www.cancerresearchuk.org/health-professional/cancer-statistics/statistics-by-cancer-type/brain-other-cns-and-intracranial-tumours#heading-Two. (Retrieved: 2023-06-16).

[7] National Cancer Institute. "Childhood cancers." (2023), [Online]. Available: https://www.cancer.gov/types/childhood-cancers. (Retrieved: 2023-06-16).

[8] Children's Hospital of Philadelphia. "Pediatric brain tumors." (2023), [Online]. Available: https://www.chop.edu/conditions-diseases/pediatric-brain-tumors. (Retrieved: 2023-06-16).

[9] O. D. Knight James and Jesus, "Pilocytic astrocytoma," 2023.

[10] I. F. Pollack, S. Agnihotri, and A. Broniscer, "Childhood brain tumors: Current management, biological insights, and future directions: Jnspg 75th anniversary invited review article," *Journal of Neurosurgery: Pediatrics*, vol. 23, no. 3, pp. 216–273, 2019.

[11] E. Nicklin, G. Velikova, C. Hulme, and et al., "Long-term issues and supportive care needs of adolescent and young adult childhood brain tumour survivors and their caregivers: A systematic review," *Psycho-oncology*, vol. 28, no. 3, pp. 477–487, 2019.

[12] M. R. Horsman and J. Overgaard, "Hyperthermia: A potent enhancer of radiotherapy," *Clinical oncology*, vol. 19, no. 6, pp. 418–426, 2007.

[13] A. Oei, H. Kok, S. Oei, and et al., "Molecular and biological rationale of hyperthermia as radio-and chemosensitizer," *Advanced drug delivery reviews*, 2020.

[14] M. Zanoli and H. Dobšíček Trefná, "Iterative time-reversal for multi-frequency hyperthermia," *Physics in Medicine & Biology*, vol. 66, no. 4, 2020. DOI: 10.1088/1361-6560/abd41a. [Online]. Available: https://pubmed.ncbi.nlm.nih.gov/33326945/.

[15] D. Stanić, D. Grujičić, T. Pekmezović, *et al.*, "Clinical profile, treatment and outcome of pediatric brain tumors in serbia in a 10-year period: A national referral institution experience," *PLoS One*, vol. 16, no. 10, e0259095, 2021.

[16] "Anatomy." Accessed: May 25, 2024, Atlanta Brain and Spine Care. (), [Online]. Available: https://www.atlantabrainandspine.com/brain-anatomy/.

[17] M. Unverdi and K. Alsayouri, "Neuroanatomy, cerebellar dysfunction," 2019.

[18] H. Basinger and J. P. Hogg, "Neuroanatomy, brainstem," 2019.

[19] D. Segal and M. A. Karajannis, "Pediatric brain tumors: An update," *Current problems in pediatric and adolescent health care*, vol. 46, no. 7, pp. 242–250, 2016.

[20] T. (Winslow, *Anatomy – nervous system: People – child*, Color, medical illustration, AV Number: CDR689771, National Cancer Institute, Nov. 2010. [Online]. Available: https://visualsonline.cancer.gov/details.cfm?imageid=9155 (visited on 04/15/2011).

[21] S. T. Jünger, B. Timmermann, and T. Pietsch, "Pediatric ependymoma: An overview of a complex disease," *Child's Nervous System*, vol. 37, no. 8, pp. 2451–2463, 2021.

[22] L. Greuter, R. Guzman, and J. Soleman, "Typical pediatric brain tumors occurring in adults—differences in management and outcome," *Biomedicines*, vol. 9, no. 4, p. 356, 2021.

[23] D.-F. C. Institute. "What are the differences between adult and childhood brain tumors?" Updated: May 24, 2017. (May 2015), [Online]. Available: https://blog.dana-farber.org/insight/2015/05/what-are-the-differences-between-adult-and-childhood-brain-tumors/ (visited on 05/24/2017).

[24] S. Keown, "Kids are not little adults," *Fred Hutch News Service*, Nov. 2016.

[25] T. E. Merchant, I. F. Pollack, and J. S. Loeffler, "Brain tumors across the age spectrum: Biology, therapy, and late effects," in *Seminars in radiation oncology*, Elsevier, vol. 20, 2010, pp. 58–66.

[26] M. Otth, J. Wyss, and K. Scheinemann, "Long-term follow-up of pediatric cns tumor survivors—a selection of relevant long-term issues," *Children*, vol. 9, no. 4, p. 447, 2022.

[27] A. Pancaldi, M. Pugliese, C. Migliozzi, J. Blom, M. Cellini, and L. Iughetti, "Neuropsychological outcomes of children treated for brain tumors," *Children*, vol. 10, no. 3, p. 472, 2023.

[28] A. R. Cohen, "Brain tumors in children," *New England Journal of Medicine*, vol. 386, no. 20, pp. 1922–1931, 2022.

[29] Y. W. Park, P. Vollmuth, M. Foltyn-Dumitru, *et al.*, "The 2021 who classification for gliomas and implications on imaging diagnosis: Part 1—key points of the fifth edition and summary of imaging findings on adult-type diffuse gliomas," *Journal of Magnetic Resonance Imaging*, vol. 58, no. 3, pp. 677–689, 2023.

[30] S. L. McGovern, D. Grosshans, and A. Mahajan, "Embryonal brain tumors," *The Cancer Journal*, vol. 20, no. 6, pp. 397–402, 2014.

[31] Cancer Research UK, *Grades of brain tumours*, https://www.cancerresearchuk.org/about-cancer/brain-tumours/grades, Accessed: May 11, 2024, 2023.

[32] Q. T. Ostrom, M. Price, C. Neff, *et al.*, "Cbtrus statistical report: Primary brain and other central nervous system tumors diagnosed in the united states in 2016—2020," *Neuro-oncology*, vol. 25, no. Supplement_4, pp. iv1–iv99, 2023.

[33] J. E. Pellot and O. De Jesus, "Diffuse intrinsic pontine glioma," in *StatPearls [Internet]*, StatPearls Publishing, 2023.

[34] N. C. Institute, *Diffuse intrinsic pontine glioma (dipg)*, Accessed: 2024-06-20, 2024. [Online]. Available: `https://www.cancer.gov/types/brain/patient/diffuse-intrinsic-pontine-glioma`.

[35] L. M. Hoffman, S. E. Veldhuijzen van Zanten, N. Colditz, *et al.*, "Clinical, radiologic, pathologic, and molecular characteristics of long-term survivors of diffuse intrinsic pontine glioma (dipg): A collaborative report from the international and european society for pediatric oncology dipg registries," *Journal of clinical oncology*, vol. 36, no. 19, pp. 1963–1972, 2018.

[36] D. N. Louis, A. Perry, P. Wesseling, *et al.*, "The 2021 who classification of tumors of the central nervous system: A summary," *Neuro-oncology*, vol. 23, no. 8, pp. 1231–1251, 2021.

[37] S. H. Torp, O. Solheim, and A. J. Skjulsvik, "The who 2021 classification of central nervous system tumours: A practical update on what neurosurgeons need to know—a minireview," *Acta Neurochirurgica*, vol. 164, no. 9, pp. 2453–2464, 2022.

[38] M. Kapoor and V. Gupta, "Astrocytoma," 2020.

[39] N. Gerges, A. M. Fontebasso, S. Albrecht, D. Faury, and N. Jabado, "Pediatric high-grade astrocytomas: A distinct neuro-oncological paradigm," *Genome medicine*, vol. 5, pp. 1–12, 2013.

[40] E. G. Shaw and J. H. Wisoff, "Prospective clinical trials of intracranial low-grade glioma in adults and children," *Neuro-oncology*, vol. 5, no. 3, pp. 153–160, 2003.

[41] B. J. Fisher, C. C. Leighton, O. Vujovic, D. R. Macdonald, and L. Stitt, "Results of a policy of surveillance alone after surgical management of pediatric low grade gliomas," *International Journal of Radiation Oncology* Biology* Physics*, vol. 51, no. 3, pp. 704–710, 2001.

[42] S. R. Burzynski, "Treatments for astrocytic tumors in children: Current and emerging strategies," *Pediatric Drugs*, vol. 8, pp. 167–178, 2006.

[43] R. J. Packer, J. M. Boyett, R. A. Zimmerman, *et al.*, "Outcome of children with brain stem gliomas after treatment with 7800 cgy of hyperfractionated radiotherapy. a childrens cancer group phase 1/11 trial," *Cancer*, vol. 74, no. 6, pp. 1827–1834, 1994.

[44] J. Fangusaro, "Pediatric high-grade gliomas and diffuse intrinsic pontine gliomas," *Journal of child neurology*, vol. 24, no. 11, pp. 1409–1417, 2009.

[45] K. K. Das and R. Kumar, "Pediatric glioblastoma," *Exon Publications*, pp. 297–312, 2017.

[46] J. Wyss, N. A. Frank, J. Soleman, and K. Scheinemann, "Novel pharmacological treatment options in pediatric glioblastoma—a systematic review," *Cancers*, vol. 14, no. 11, p. 2814, 2022.

[47] S. M. Elwatidy, J. Ahmed, M. H. Bawazir, *et al.*, "Outcome of childhood cerebellar pilocytic astrocytoma: A series with 20 years of follow up," *Cureus*, vol. 14, no. 2, 2022.

[48] M. Ansari, H. Nasrolahi, A.-A. Kani, *et al.*, "Pediatric glioblastoma multiforme: A single-institution experience," *Indian Journal of Medical and Paediatric Oncology*, vol. 33, no. 03, pp. 155–160, 2012.

[49] N. Jovanovich, A. Habib, J. Head, F. Hameed, S. Agnihotri, and P. O. Zinn, "Pediatric diffuse midline glioma: Understanding the mechanisms and assessing the next generation of personalized therapeutics," *Neuro-Oncology Advances*, vol. 5, no. 1, vdad040, 2023.

[50] S. Damodharan, M. Lara-Velazquez, B. C. Williamsen, J. Helgager, and M. Dey, "Diffuse intrinsic pontine glioma: Molecular landscape, evolving treatment strategies and emerging clinical trials," *Journal of Personalized Medicine*, vol. 12, no. 5, p. 840, 2022.

[51] Brain Tumor Charity, *Diffuse midline glioma (dipg) prognosis*, Accessed: 2024-06-07, 2024. [Online]. Available: `https://www.thebraintumourcharity.org/`.

[52] Brain Tumor Research, *Diffuse midline glioma*, Accessed: 2024-06-07, 2024. [Online]. Available: `https://www.braintumourresearch.org/`.

[53] J. S. Rechberger, V. M. Lu, L. Zhang, E. A. Power, and D. J. Daniels, "Clinical trials for diffuse intrinsic pontine glioma: The current state of affairs," *Child's Nervous System*, vol. 36, pp. 39–46, 2020.

[54] T. E. Dick, D. M. Baekey, J. F. Paton, B. G. Lindsey, and K. F. Morris, "Cardio-respiratory coupling depends on the pons," *Respiratory physiology & neurobiology*, vol. 168, no. 1-2, pp. 76–85, 2009.

[55] W. M. Rashed, E. Maher, M. Adel, O. Saber, and M. S. Zaghloul, "Pediatric diffuse intrinsic pontine glioma: Where do we stand?" *Cancer and Metastasis Reviews*, vol. 38, no. 4, pp. 759–770, 2019.

[56] K. J. Cohen, N. Jabado, and J. Grill, "Diffuse intrinsic pontine gliomas—current management and new biologic insights. is there a glimmer of hope?" *Neuro-oncology*, vol. 19, no. 8, pp. 1025–1034, 2017.

[57] M. I. Vanan and D. D. Eisenstat, "Dipg in children–what can we learn from the past?" *Frontiers in oncology*, vol. 5, p. 237, 2015.

[58] F. J. Rodriguez, T. Tihan, D. Lin, *et al.*, "Clinicopathologic features of pediatric oligodendrogliomas: A series of 50 patients," *The American journal of surgical pathology*, vol. 38, no. 8, pp. 1058–1070, 2014.

[59] M. Bradl and H. Lassmann, "Oligodendrocytes: Biology and pathology," *Acta neuropathologica*, vol. 119, pp. 37–53, 2010.

[60] L. Byer, C. Kline-Nunnally, T. Tihan, and S. Mueller, "Pediatric oligodendroglioma," in *Oligodendroglioma*, Elsevier, 2019, pp. 379–386.

[61] F. M. Mezzacappa and W. Thorell, "Neuronal brain tumors," in *StatPearls [Internet]*, StatPearls Publishing, 2022.

[62] J. H. Shin, H. K. Lee, S. K. Khang, *et al.*, "Neuronal tumors of the central nervous system: Radiologic findings and pathologic correlation," *Radiographics*, vol. 22, no. 5, pp. 1177–1189, 2002.

[63] J. Zentner, H. K. Wolf, B. Ostertun, *et al.*, "Gangliogliomas: Clinical, radiological, and histopathological findings in 51 patients.," *Journal of Neurology, Neurosurgery & Psychiatry*, vol. 57, no. 12, pp. 1497–1502, 1994.

[64] M. K. Demir, O. Yapıcıer, B. Yılmaz, and T. Kılıç, "Magnetic resonance imaging findings of mixed neuronal–glial tumors with pathologic correlation: A review," *Acta Neurologica Belgica*, vol. 118, pp. 379–386, 2018.

[65] J. M. Provenzale, U. Ali, D. P. Barboriak, D. F. Kallmes, D. M. Delong, and R. E. McLendon, "Comparison of patient age with mr imaging features of gangliogliomas," *American Journal of Roentgenology*, vol. 174, no. 3, pp. 859–862, 2000.

[66] L. Kumar, S. F. A. Deepa, I. Moinca, P. Suresh, and K. R. Naidu, "Medulloblastoma: A common pediatric tumor: Prognostic factors and predictors of outcome," *Asian Journal of Neurosurgery*, vol. 10, no. 01, pp. 50–50, 2015.

[67] N. E. Millard and K. C. De Braganca, "Medulloblastoma," *Journal of child neurology*, vol. 31, no. 12, pp. 1341–1353, 2016.

[68] S. Mahapatra and M. J. Amsbaugh, "Medulloblastoma," 2017.

[69] N. Nalita, S. Ratanalert, K. Kanjanapradit, T. Chotsampancharoen, and T. Tunthanathip, "Survival and prognostic factors in pediatric patients with medulloblastoma in southern thailand," *Journal of Pediatric Neurosciences*, vol. 13, no. 2, pp. 150–157, 2018.

[70] M. Park, J. W. Han, S. M. Hahn, *et al.*, "Atypical teratoid/rhabdoid tumor of the central nervous system in children under the age of 3 years," *Cancer Research and Treatment: Official Journal of Korean Cancer Association*, vol. 53, no. 2, p. 378, 2021.

[71] P. P. T. E. Board, "Childhood central nervous system atypical teratoid/rhabdoid tumor treatment (pdq®)," in *PDQ Cancer Information Summaries [Internet]*, National Cancer Institute (US), 2008.

[72] C. S. Lau, K. Mahendraraj, and R. S. Chamberlain, "Atypical teratoid rhabdoid tumors: A population-based clinical outcomes study involving 174 patients from the surveillance, epidemiology, and end results database (1973–2010)," *Cancer Management and Research*, pp. 301–309, 2015.

[73] R. Rudà, F. Bruno, A. Pellerino, and R. Soffietti, "Ependymoma: Evaluation and management updates," *Current Oncology Reports*, vol. 24, no. 8, pp. 985–993, 2022.

[74] A. Stermann, N. Huebener, D. Seidel, *et al.*, "Targeting of mycn by means of dna vaccination is effective against neuroblastoma in mice," *Cancer Immunology, Immunotherapy*, vol. 64, pp. 1215–1227, 2015.

[75] A. Poretti, A. Meoded, and T. A. Huisman, "Neuroimaging of pediatric posterior fossa tumors including review of the literature," *Journal of magnetic resonance imaging*, vol. 35, no. 1, pp. 32–47, 2012.

[76] N. A. Vitanza and S. Partap, "Pediatric ependymoma," *Journal of child neurology*, vol. 31, no. 12, pp. 1354–1366, 2016.

[77] M.-c. Fan, W. Fang, K. Liu, *et al.*, "Paediatric intracranial meningiomas: Eight-year experience with 32 cases," *Chinese Neurosurgical Journal*, vol. 3, no. 03, pp. 150–153, 2017.

[78] W. He, Z. Liu, H. Teng, *et al.*, "Pediatric meningiomas: 10-year experience with 39 patients," *Journal of Neuro-Oncology*, vol. 149, pp. 543–553, 2020.

[79] A. Stanuszek, P. Piątek, S. Kwiatkowski, and D. Adamek, "Multiple faces of children and juvenile meningiomas: A report of single-center experience and review of literature," *Clinical neurology and neurosurgery*, vol. 118, pp. 69–75, 2014.

[80] A. Tauziède-Espariat, S. M. Pfister, C. Mawrin, and F. Sahm, "Pediatric meningiomas: A literature review and diagnostic update," *Neuro-oncology advances*, vol. 5, no. Supplement_1, pp. i105–i111, 2023.

[81] I. Opoku, L. Yang, P. Sun, *et al.*, "Pediatric cerebral meningioma: A single-center study with 10 children not associated with neurofibromatosis type 2 and literature review," *Pediatric Neurosurgery*, vol. 57, no. 6, pp. 422–433, 2023.

[82] M. Ortiz Torres, I. Shafiq, and F. Mesfin, "Pediatric craniopharyngioma," *StatPearls [Internet]*, Apr. 2023. [Online]. Available: `https://www.ncbi.nlm.nih.gov/books/NBK519027/`.

[83] A. Drapeau, P. C. Walz, J. G. Eide, *et al.*, "Pediatric craniopharyngioma," *Child's Nervous System*, vol. 35, pp. 2133–2145, 2019.

[84] H. L. Müller, "Craniopharyngioma," *Endocrine reviews*, vol. 35, no. 3, pp. 513–543, 2014.

[85] L. M. Hoffman, C. Jaimes, K. Mankad, *et al.*, "Response assessment in pediatric craniopharyngioma: Recommendations from the response assessment in pediatric neuro-oncology (rapno) working group," *Neuro-oncology*, vol. 25, no. 2, pp. 224–233, 2023.

[86] M. Jensterle, S. Jazbinsek, R. Bosnjak, *et al.*, "Advances in the management of craniopharyngioma in children and adults," *Radiology and oncology*, vol. 53, no. 4, pp. 388–396, 2019.

[87] E. J. Koh, K.-C. Wang, J. H. Phi, *et al.*, "Clinical outcome of pediatric choroid plexus tumors: Retrospective analysis from a single institute," *Child's Nervous System*, vol. 30, pp. 217–225, 2014.

[88] P. Strojan, M. Popovic, K. Surlan, and B. Jereb, "Choroid plexus tumors: A review of 28-year experience," *Neoplasma*, vol. 51, no. 4, pp. 306–312, 2004.

[89] A. Osborn, D. Louis, T. Poussaint, L. Linscott, and K. Salzman, "The 2021 world health organization classification of tumors of the central nervous sys-

tem: What neuroradiologists need to know," *American Journal of Neuroradiology*, vol. 43, no. 7, pp. 928–937, 2022.

[90] N. Gupta, "Choroid plexus tumors in children," *Neurosurgery Clinics*, vol. 14, no. 4, pp. 621–631, 2003.

[91] J. Wolff, M. Sajedi, R. Brant, M. Coppes, and R. Egeler, "Choroid plexus tumours," *British journal of cancer*, vol. 87, no. 10, pp. 1086–1091, 2002.

[92] S. Lam, Y. Lin, J. Cherian, *et al.*, "Choroid plexus tumors in children: A population-based study," *Pediatric neurosurgery*, vol. 49, no. 6, pp. 331–338, 2015.

[93] A. L. Slingerland, J. E. Papadakis, S. J. Staffa, *et al.*, "Management of choroid plexus tumors and the benefit of preoperative embolization in pediatric patients: Report of 46 cases from a single institution," *World Neurosurgery*, vol. 181, e1071–e1087, 2024.

[94] J. W. Oosterhuis and L. H. Looijenga, "Human germ cell tumours from a developmental perspective," *Nature Reviews Cancer*, vol. 19, no. 9, pp. 522–537, 2019.

[95] A. Zhang and Y. Gao, "Intracranial germ cell tumors in pediatric and adolescent patients in china: Systematic review and meta-analysis," *Pediatric Medicine*, vol. 5, 2022.

[96] M. E. Echevarría, J. Fangusaro, and S. Goldman, "Pediatric central nervous system germ cell tumors: A review," *The oncologist*, vol. 13, no. 6, pp. 690–699, 2008.

[97] Z. Kong, Y. Wang, C. Dai, Y. Yao, W. Ma, and Y. Wang, "Central nervous system germ cell tumors: A review of the literature," *Journal of child neurology*, vol. 33, no. 9, pp. 610–620, 2018.

[98] K. K. Yeo, S. Nagabushan, G. Dhall, and M. S. Abdelbaki, "Primary central nervous system germ cell tumors in children and young adults: A review of controversies in diagnostic and treatment approach," *Neoplasia*, vol. 36, p. 100 860, 2023.

[99] A. Tauziède-Espariat, L. Hasty, A. Métais, and P. Varlet, "Mesenchymal non-meningothelial tumors of the central nervous system: A literature review and diagnostic update of novelties and emerging entities," *Acta Neuropathologica Communications*, vol. 11, no. 1, p. 22, 2023.

[100] M. C. Mancini *et al.*, "Lymphomas, endocrine, mesenchymal, and other rare tumors of the mediastinum treatment & management," *Medscape*, 2021, Updated: Feb 16, 2021.

[101] A. Ages, "Childhood soft tissue sarcoma treatment (pdq®) health professional version,"

[102] S. M. Lim, C. J. Yoo, J. W. Han, *et al.*, "Incidence and survival of pediatric soft tissue sarcomas: Comparison between adults and children," *Cancer research and treatment: official journal of Korean Cancer Association*, vol. 47, no. 1, p. 9, 2015.

[103] F. Guedes, R. S. Brown, F. J. L. Torrão-Junior, D. A. Barbosa, G. d. A. G. Ravanini, and R. M. P. Amorim, "Pediatric peripheral nerve tumors: Clinical and surgical aspects," *Child's Nervous System*, vol. 35, pp. 2289–2297, 2019.

[104] C. Clinic, "Nerve sheath tumor," *Cleveland Clinic*, 2022, Medically Reviewed. Last reviewed on March 14, 2022.
[105] M. Bienkowski, J. Furtner, and J. A. Hainfellner, "Clinical neuropathology of brain tumors," *Handbook of clinical neurology*, vol. 145, pp. 477–534, 2018.
[106] L. Messersmith and K. Krauland, "Neurofibroma," 2019.
[107] National Cancer Institute, "Schwannoma," Jul. 2020.
[108] J. M. Miller, N. Morrell, and R. H. Quinn. "Hemangioma." Last reviewed August 2018. Contributed and/or updated by James M. Miller, BS; Nathan Morrell, MD; Robert H. Quinn, MD. Peer-reviewed by Rajiv Rajani, MD; Stuart J. Fischer, MD. (Aug. 2018), [Online]. Available: `https://orthoinfo.aaos.org/en/diseases--conditions/hemangioma`.
[109] T. Refaat, S. Sachdev, V. Sathiaseelan, *et al.*, "Hyperthermia and radiation therapy for locally advanced or recurrent breast cancer," *The Breast*, vol. 24, no. 4, pp. 418–425, 2015.
[110] R. Issels, E. Kampmann, R. Kanaar, and L. H. Lindner, "Hallmarks of hyperthermia in driving the future of clinical hyperthermia as targeted therapy: Translation into clinical application," *International Journal of Hyperthermia*, vol. 32, no. 1, pp. 89–95, 2016.
[111] G. Y. Yi, M. J. Kim, H. I. Kim, J. Park, and S. H. Baek, "Hyperthermia treatment as a promising anti-cancer strategy: Therapeutic targets, perspective mechanisms and synergistic combinations in experimental approaches," *Antioxidants*, vol. 11, no. 4, p. 625, 2022.
[112] J. Crezee, N. A. Franken, and A. L. Oei, *Hyperthermia-based anti-cancer treatments*, 2021.
[113] J. Vrba, M. Lapeš, and L. Oppl, "Technical aspects of microwave thermotherapy," *Bioelectrochemistry and bioenergetics*, vol. 48, no. 2, pp. 305–309, 1999.
[114] H. D. Trefna, J. Crezee, and P. Kok, "Delivering energy using localized hyperthermia systems," *The Application of Heat in Oncology: Principles and Practice*, pp. 73–94, 2023.
[115] S. Kwon, S. Jung, and S. H. Baek, "Combination therapy of radiation and hyperthermia, focusing on the synergistic anti-cancer effects and research trends," *Antioxidants*, vol. 12, no. 4, p. 924, 2023.
[116] M. G. Aram, *Antenna Design, Radiobiological Modelling, and Non-Invasive Monitoring for Microwave Hyperthermia*. Chalmers Tekniska Hogskola (Sweden), 2022.
[117] M. Ghaderi Aram, M. Zanoli, H. Nordström, I. Toma-Dasu, K. Blomgren, and H. Dobšíček Trefná, "Radiobiological evaluation of combined gamma knife radiosurgery and hyperthermia for pediatric neuro-oncology," *Cancers*, vol. 13, no. 13, p. 3277, 2021.
[118] H. H. Pennes, "Analysis of tissue and arterial blood temperatures in the resting human forearm," *Journal of applied physiology*, vol. 1, no. 2, pp. 93–122, 1948.
[119] M. Zanoli and H. Dobšíček Trefná, "The hot-to-cold spot quotient for sar-based treatment planning in deep microwave hyperthermia," *International Journal of Hyperthermia*, vol. 39, no. 1, pp. 1421–1439, 2022. DOI: `0.1080/02656736.2022.2136411`.

[120] H. K. Lee, A. G. Antell, C. A. Perez, et al., "Superficial hyperthermia and irradiation for recurrent breast carcinoma of the chest wall: Prognostic factors in 196 tumors," *International journal of radiation oncology, biology, physics*, vol. 40, no. 2, pp. 365–375, 1998.

[121] G. G. Bellizzi, T. Drizdal, G. C. van Rhoon, L. Crocco, T. Isernia, and M. M. Paulides, "Predictive value of sar based quality indicators for head and neck hyperthermia treatment quality," *International journal of hyperthermia: the official journal of European Society for Hyperthermic Oncology, North American Hyperthermia Group*, vol. 36, no. 1, pp. 456–465, 2019. DOI: 10.1080/02656736.2019.1590652.

[122] A. Bakker, J. van der Zee, G. van Tienhoven, H. P. Kok, C. R. Rasch, and H. Crezee, "Temperature and thermal dose during radiotherapy and hyperthermia for recurrent breast cancer are related to clinical outcome and thermal toxicity: A systematic review," *International Journal of Hyperthermia*, vol. 36, no. 1, pp. 1023–1038, 2019.

[123] M. M. Paulides, S. H. Vossen, A. P. Zwamborn, and G. C. van Rhoon, "Theoretical investigation into the feasibility to deposit rf energy centrally in the head-and-neck region," *International Journal of Radiation Oncology, Biology, Physics*, vol. 63, no. 2, pp. 634–642, 2005, ISSN: 0360-3016. DOI: https://doi.org/10.1016/j.ijrobp.2005.04.048. [Online]. Available: https://www.sciencedirect.com/science/article/pii/S0360301605008242.

[124] B. Guérin, J. F. Villena, A. G. Polimeridis, *et al.*, "Computation of ultimate sar amplification factors for radiofrequency hyperthermia in non-uniform body models: Impact of frequency and tumour location," *International Journal of Hyperthermia*, vol. 34, no. 1, pp. 87–100, 2018. DOI: 10.1080/02656736.2017.1319077.

[125] P. Takook, M. Persson, and H. D. Trefná, "Performance evaluation of hyperthermia applicators to heat deep-seated brain tumors," *IEEE Journal of Electromagnetics, RF and Microwaves in Medicine and Biology*, vol. 2, no. 1, pp. 18–24, 2018. DOI: 10.1109/JERM.2018.2808678.

[126] E. Oberacker, A. Kuehne, C. Oezerdem, *et al.*, "Radiofrequency applicator concepts for thermal magnetic resonance of brain tumors at 297 mhz (7.0 tesla)," *International journal of hyperthermia : the official journal of European Society for Hyperthermic Oncology, North American Hyperthermia Group*, vol. 37, no. 1, pp. 549–563, 2020. DOI: 10.1080/02656736.2020.1761462.

[127] O. E, D. C, N. J, *et al.*, "Patient-specific planning for thermal magnetic resonance of glioblastoma multiforme," *Cancers*, vol. 13, no. 8, 2021. DOI: 10.3390/cancers13081867.

[128] J. Redr, T. Pokorny, T. Drizdal, *et al.*, "Microwave hyperthermia of brain tumors: A 2d assessment parametric numerical study," *Sensors*, vol. 22, no. 16, 2022, ISSN: 1424-8220. [Online]. Available: https://www.mdpi.com/1424-8220/22/16/6115.

[129] K. D. Paulsen, S. Geimer, J. Tang, and W. E. Boyse, "Optimization of pelvic heating rate distributions with electromagnetic phased arrays," *International*

Journal of Hyperthermia, vol. 15, no. 3, pp. 157–186, 1999. DOI: 10.1080/026567399285701.

[130] M. Seebass, R. Beck, J. Gellermann, J. Nadobny, and P. Wust, "Electromagnetic phased arrays for regional hyperthermia: Optimal frequency and antenna arrangement," *International journal of hyperthermia: the official journal of European Society for Hyperthermic Oncology, North American Hyperthermia Group*, vol. 17, no. 4, pp. 321–336, 2001. DOI: 10.1080/02656730110049529.

[131] G. G. Bellizzi, K. Sumser, and M. T. Bevacqua, "On the optimal matching medium and the working frequency in deep pelvic hyperthermia," *IEEE Journal of Electromagnetics, RF and Microwaves in Medicine and Biology*, vol. 5, no. 3, pp. 223–230, 2021. DOI: 10.1109/JERM.2020.3047980.

[132] M. Zanoli, E. Ek, and H. Dobšíček Trefná, "Antenna arrangement in UWB helmet brain applicators for deep microwave hyperthermia," *Cancers*, vol. 15, no. 5, 2023, ISSN: 2072-6694. DOI: 10.3390/cancers15051447. [Online]. Available: https://www.mdpi.com/2072-6694/15/5/1447.

[133] W. T. Joines, Y. Zhang, C. Li, and R. L. Jirtle, "The measured electrical properties of normal and malignant human tissues from 50 to 900 mhz," *Medical physics*, vol. 21, no. 4, pp. 547–550, 1994. DOI: 10.1118/1.597312.

[134] P. Hasgall, F. Di Gennaro, C. Baumgartner, *et al.*, "IT'IS Database for thermal and electromagnetic parameters of biological tissues," Version 4.1, Feb 22, 2022. DOI: 10.13099/VIP21000-04-1.

[135] IT'IS Foundation. "Human models." (2024), [Online]. Available: https://itis.swiss/virtual-population/virtual-population/overview/. (Retrieved: 2024-04-10).

[136] M. Waqar, D. Lewis, E. Agushi, M. Gittins, A. Jackson, and D. Coope, "Cerebral and tumoral blood flow in adult gliomas: A systematic review of results from magnetic resonance imaging," *The British Journal of Radiology*, vol. 94, no. 1125, 2021. DOI: 10.1259/bjr.20201450.

A

Appendix

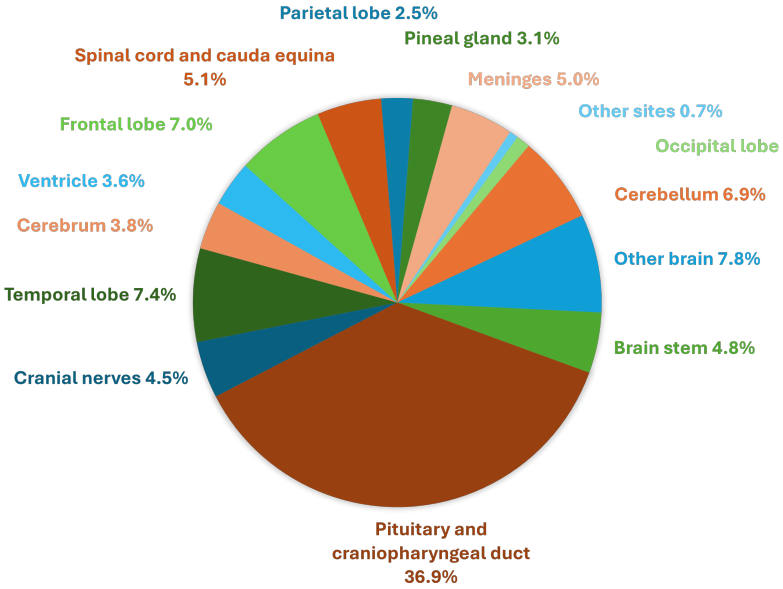

Figure A.1: Distribution of primary brain and other CNS tumor in age group, 15 – 19, by anatomical site from CBTRUS statistical report: NPCR and SEER, 2016 – 2020 [32]

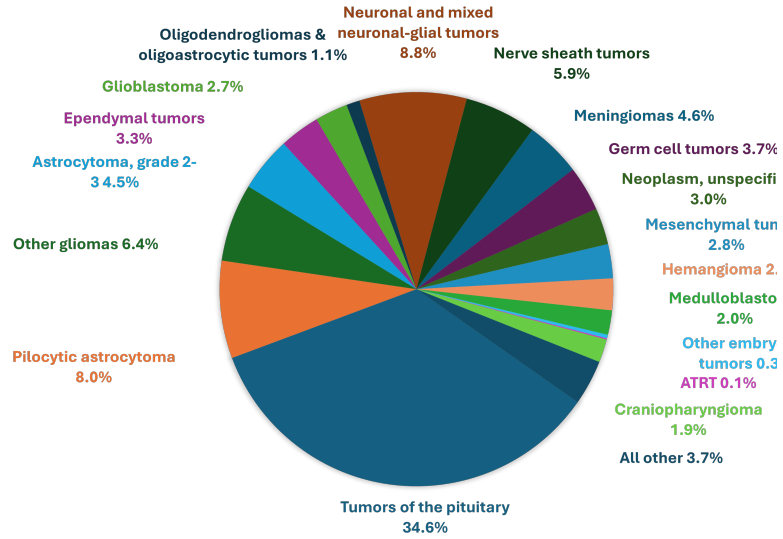

Figure A.2: Distribution of primary brain and other CNS tumor in age group, 15 – 19, based on histopathology subtypes with data from CBTRUS statistical report: NPCR and SEER, 2016 – 2020 [32].

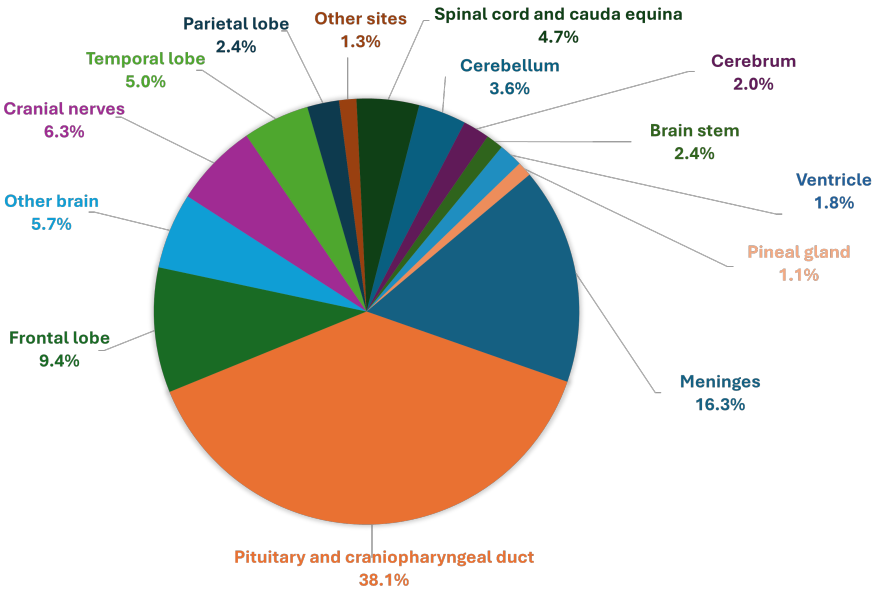

Figure A.3: Distribution of primary brain and other CNS tumor in adolescents and young adults, 15 – 39 years by anatomical site from CBTRUS statistical report: NPCR and SEER, 2016 – 2020 [32]

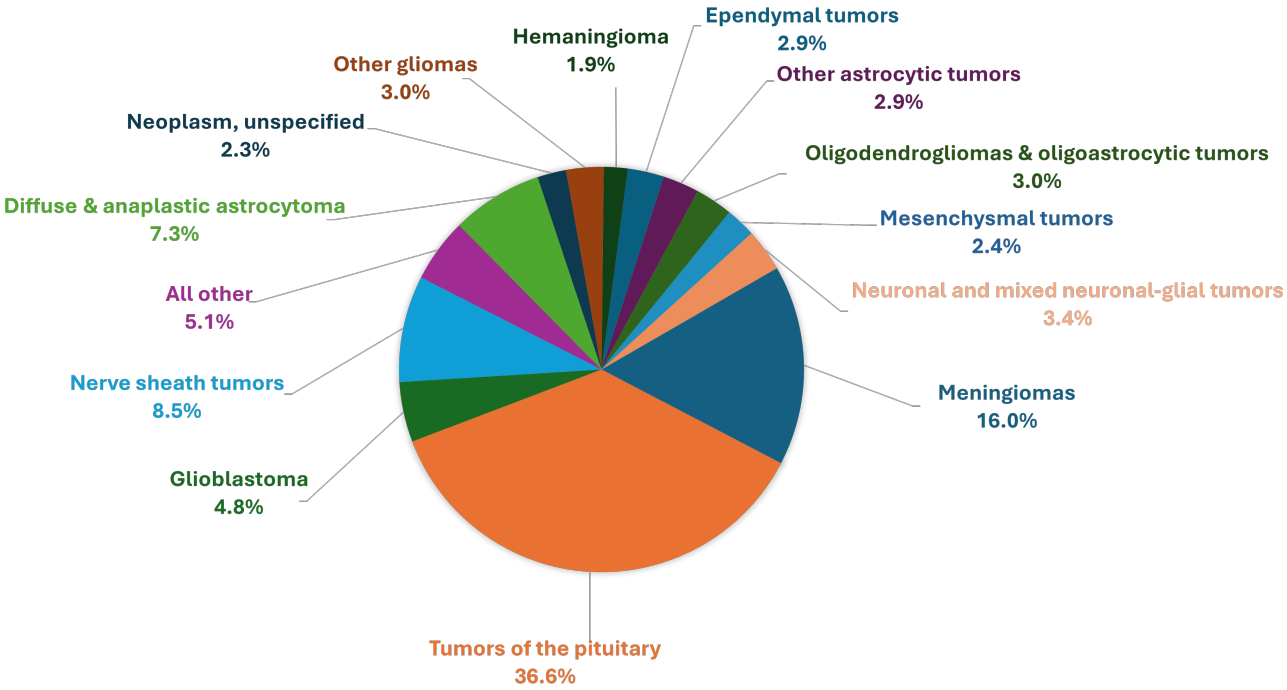

Figure A.4: Distribution of primary brain and other CNS tumor in adolescents and young adults, 15 – 39 years, by histopathology subtypes using data from CBTRUS statistical report: NPCR and SEER, 2016 – 2020 [32].

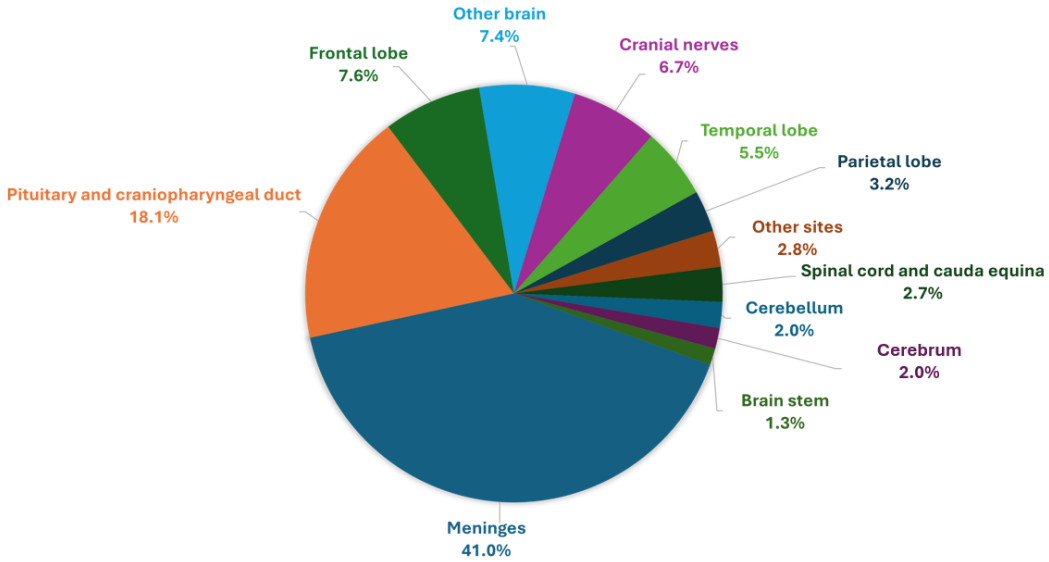

Figure A.5: Distribution of primary brain and other CNS tumor for all age groups by anatomical site from CBTRUS statistical report: NPCR and SEER, 2016 – 2020 [32]

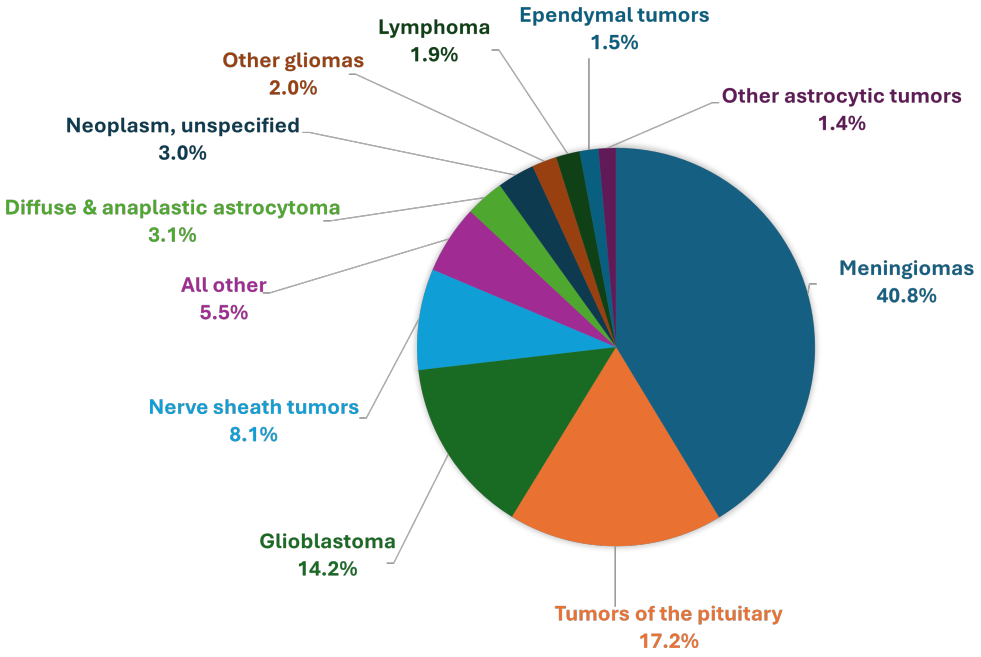

Figure A.6: Distribution of primary brain and other CNS tumor for all age groups by histopathology subtypes using data from CBTRUS statistical report: NPCR and SEER, 2016 – 2020 [32].

Color	Material
	Background
	Air
	Blood
	Brain (Grey Matter)
	Brain (White Matter)
	Cartilage
	Cerebellum
	Cerebrospinal Fluid
	Connective Tissue
	Cartilage
	Skin
	Eye (Vitreous Humor)
	Eye (Lens)
	Fat
	Hippocampus
	Hypophysis
	Hypothalamus
	Vertebrae
	Larynx
	Mandible
	Bone Marrow
	Midbrain
	Muscle
	Bone (Cortical)
	Mucous Membrane

Color	Material
	Nerve
	Pharynx
	Skin
	Skull Cortical
	Spinal cord
	SAT (Subcutaneous Fat)
	Tooth
	Tendon-Ligament
	Thalamus
	Tongue
	Blood
	Vertebrae
	Pineal Body
	Pons
	Medulla Oblongata
	Eye (Cornea)
	Eye (Sclera)
	Esophagus
	Esophagus Lumen
	Lung
	Thyroid Gland
	Trachea
	Trachea Lumen
	Tumor target

Table A.1: Material with their respective color for the Billie model, case 1.

Color	Material
	Skin
	Muscle
	Bone (Cortical)
	Pharynx
	Cerebrospinal fluid
	Brain (Grey matter)
	Brain (White matter)
	Tumor
	Eye (Vitreous humor)
	Cartilage

Table A.2: Material with their respective color for the child model with medulloblastoma, case 2.

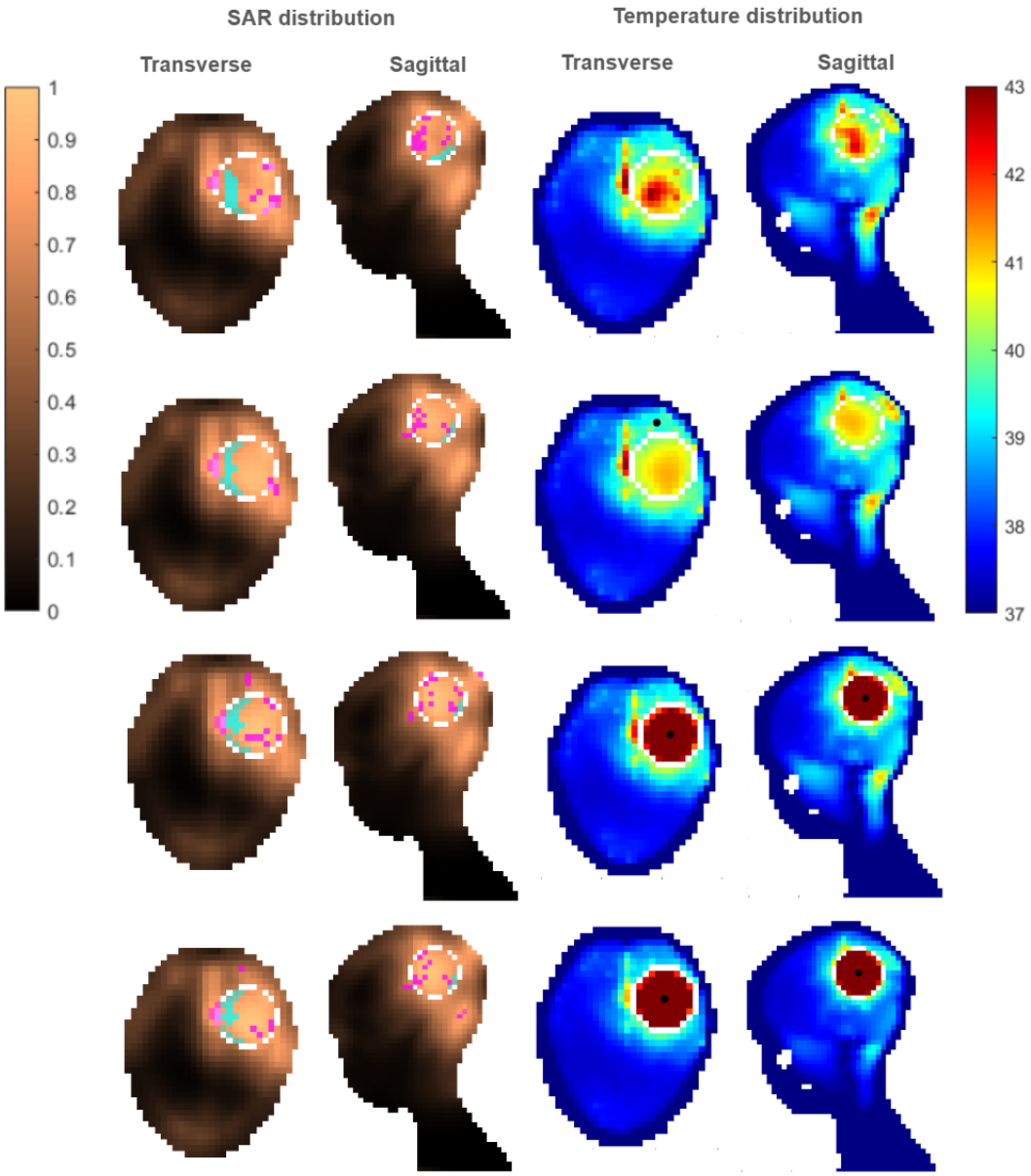

Figure A.7: SAR and temperature distributions at 275 MHz for ependymoma using all target tissue types. Shown as transverse and sagittal section at tumor center for healthy tissue (top row), average tissue, tumor (benchmark) and tumor (Schooneveldt) (bottom row). Target outlined in white. Magenta and cyan in the SAR maps represent hot and cold spots respectively. The black point in the temperature maps represents the highest temperature.

DEPARTMENT OF ELECTRICAL ENGINEERING
CHALMERS UNIVERSITY OF TECHNOLOGY
Gothenburg, Sweden
www.chalmers.se

CHALMERS
UNIVERSITY OF TECHNOLOGY